A Dual-Frequency Radar Retrieval of Two Parameters of the Snowfall Particle Size Distribution Using a Neural Network

RANDY J. CHASE,[a] STEPHEN W. NESBITT,[a] AND GREG M. MCFARQUHAR[b,c]

[a] *Department of Atmospheric Sciences, University of Illinois at Urbana–Champaign, Urbana, Illinois*
[b] *Cooperative Institute of Mesoscale Meteorological Studies, University of Oklahoma, Norman, Oklahoma*
[c] *School of Meteorology, University of Oklahoma, Norman, Oklahoma*

(Manuscript received 12 August 2020, in final form 18 November 2020)

ABSTRACT: With the launch of the Global Precipitation Measurement Dual-Frequency Precipitation Radar (GPM-DPR) in 2014, renewed interest in retrievals of snowfall in the atmospheric column has occurred. The current operational GPM-DPR retrieval largely underestimates surface snowfall accumulation. Here, a neural network (NN) trained on data that are synthetically derived from state-of-the-art ice particle scattering models and measured in situ particle size distributions (PSDs) is used to retrieve two parameters of the PSD: liquid equivalent mass-weighted mean diameter D_{mi} and the liquid equivalent normalized intercept parameter N_{wi}. Evaluations against a test dataset showed statistically significantly improved ice water content (IWC) retrievals relative to a standard power-law approach and an estimate of the current GPM-DPR algorithm. Furthermore, estimated median percent errors (MPE) on the test dataset were −0.7%, +2.6%, and +1% for D_{mi}, N_{wi}, and IWC, respectively. An evaluation on three case studies with collocated radar observations and in situ microphysical data shows that the NN retrieval has MPE of −13%, +120%, and +10% for D_{mi}, N_{wi}, and IWC, respectively. The NN retrieval applied directly to GPM-DPR data provides improved snowfall retrievals relative to the default algorithm, removing the default algorithm's ray-to-ray instabilities and recreating the high-resolution radar retrieval results to within 15% MPE. Future work should aim to improve the retrieval by including PSD data collected in more diverse conditions and rimed particles. Furthermore, different desired outputs such as the PSD shape parameter and snowfall rate could be included in future iterations.

KEYWORDS: Snowfall; Ice particles; Aircraft observations; Radars/Radar observations; Remote sensing; Neural networks

1. Introduction

Despite being confined to high latitudes and altitudes when occurring at the surface, snow can be related to approximately 50% by number (Field and Heymsfield 2015) and approximately 60% by mass accumulation (Heymsfield et al. 2020) of all precipitation across cold and warm climates. Thus, the accurate retrieval of snow properties is required for an accurate quantification of the hydrologic cycle. Furthermore, the quantitative retrieval of snowfall properties is invaluable for the evaluation of atmospheric numerical model simulations and their parameterized ice-phase microphysics (e.g., Delanoë et al. 2011; Stein et al. 2015; Ori et al. 2020). Despite many advances in satellite remote sensing techniques and sensors in the past few decades, the uncertainty in the estimate of the atmosphere's ice water path remains large, and there is poor agreement between observational retrievals and numerical models (e.g., Duncan and Eriksson 2018).

The best way to retrieve global snowfall properties is to use spaceborne microwave radars since ground-based observations are limited to easily accessible locations and passive spaceborne sensors have additional ambiguity in determining the vertical distribution of hydrometeors. Currently, there exist two NASA missions with spaceborne radars designed to sample hydrometeors. The first mission, launched in 2006, is *CloudSat* (Stephens et al. 2002), which consists of a highly sensitive 94 GHz nonscanning cloud radar in a 98° inclination orbit. The second mission, starting in 2014, is the Global Precipitation Measurement mission (GPM; Hou et al. 2014), which operates the Dual-Frequency Precipitation Radar (DPR; 13.5 and 35.5 GHz) in a 65° inclination orbit. Both satellites have collected observations of equivalent radar reflectivity factor Z_e in a variety of snowfall over their missions.

To retrieve snowfall properties, namely snowfall rate S, the most common method has been the use of a prescribed power-law relation between Z_e and S that takes the form

$$Z_e = \alpha S^{\beta}. \tag{1}$$

The parameters in Eq. (1), α and β, are typically derived from direct comparisons of observed Z_e and S (e.g., Langille and Thain 1951; Boucher and Wieler 1985; Fujiyoshi et al. 1990), theoretical particle scattering models (e.g., Liu 2008; Kulie and Bennartz 2009), or a combination of both (e.g., Matrosov 1992;

Chase's current affiliations: School of Computer Science, and School of Meteorology, University of Oklahoma, Norman, Oklahoma.

Corresponding author: Randy J. Chase, randychase@ou.edu

DOI: 10.1175/JAMC-D-20-0177.1

von Lerber et al. 2017). The direct comparison of observed Z_e and S is sensitive to the radar's calibration and operating frequency, as well as intrinsic particle properties including the large observed variability in particle size distributions, crystal habits, and degrees of riming, making it difficult to find a relation that can be applied universally. The use of theoretical scattering models (e.g., Mie theory; T matrix; discrete dipole approximation) is largely dependent on the microphysical assumptions made within them, leading uncertainties in the estimate of S up to a factor of 10 (Hiley et al. 2011). Thus, it should be clear that in order to improve the estimate of global snowfall properties, methods beyond using a single standard power-law fit must be explored.

Currently, the operational retrieval method used in *CloudSat* uses optimal estimation (Rodgers 2000), where the observed Z_e and a priori constraints are used to retrieve snowfall properties (Wood et al. 2013; Wood and L'Ecuyer 2021). Since this method has shown good agreement with ground-based radar retrievals in the United States (Cao et al. 2014; Chen et al. 2016), Sweden (Norin et al. 2015), and Antarctica (Souverijns et al. 2018), *CloudSat* is currently considered the best estimate of global snowfall properties and has been used in numerous snowfall investigations (e.g., Palerme et al. 2014; Kulie et al. 2016; Palerme et al. 2017; Milani et al. 2018; Kulie and Milani 2018; Kulie et al. 2020). The uncertainty in *CloudSat*'s retrieval of S has improved with the optimal estimation technique relative to a single power-law fit, although the retrieval has nontrivial uncertainties estimated to be between 50% (Palerme et al. 2014) and 160% (Kulie et al. 2020).

To retrieve snowfall properties from GPM-DPR, an algorithm is used that prescribes a relation between the precipitation rate, mass-weighted mean diameter D_m and Z_e to simultaneously retrieve the properties of hydrometeors regardless of phase (Kozu et al. 2009; Iguchi et al. 2018). Direct comparisons between GPM-DPR snowfall retrievals and surface-based references have yet to be conducted, but the snowfall retrievals have still been used to investigate the global distribution of snowfall (e.g., Adhikari et al. 2018; Adhikari and Liu 2019). However, a comparison using *CloudSat* as a reference has shown that GPM-DPR's retrieval of global average snowfall rate is underestimated by approximately 43% even after considering measurement differences between *CloudSat* and GPM-DPR (Skofronick-Jackson et al. 2019). Furthermore, an investigation of the GPM-DPR retrieval microphysical assumptions by Chase et al. (2020) showed that the current GPM-DPR algorithm is likely inappropriate for snowfall retrievals and thus other retrieval methods should be investigated.

One alternative retrieval method for GPM-DPR is to adopt the same optimal estimation technique as *CloudSat* but at GPM-DPR frequencies. This has been shown to work well for triple-frequency observations from field campaigns (Grecu et al. 2018; Leinonen et al. 2018; Tridon et al. 2019) and could potentially be applied to dual-frequency observations. A second method, explored in this paper, would be to use an artificial neural network (NN) to retrieve snowfall properties.

Neural networks have been widely used in remote sensing (Mas and Flores 2008), including the classification of clouds from passive satellite irradiances (e.g., Key et al. 1989) as well as the retrieval of snowfall properties (e.g., Xiao et al. 1998; Sekelsky et al. 1999). Xiao et al. (1998) trained several NNs using the vertical column of single-frequency radar measurements and ground based measured snowfall accumulations, showing that the NN can perform better than the standard power-law approach. In Sekelsky et al. (1999), an NN was trained on scattering simulations produced by a T-matrix code (Mishchenko and Travis 1998) at three frequencies (S, Ka, and W bands) and a range of theoretical negative exponential distributions of particles in order to retrieve the volume weighted mean diameter D_0 and the negative exponential intercept parameter N_0. Since the study by Sekelsky et al. (1999), comparisons with more accurate numerical modeling of ice particle scattering, namely the discrete dipole approximation (DDA; Yurkin and Hoekstra 2011), have shown that T matrix predicted scattering properties cannot fully reproduce 94 GHz scattering properties of aggregates (Kneifel et al. 2011). Furthermore, the results from Sekelsky et al. (1999) were never evaluated against observations and thus the uncertainties of the retrieval are unquantified and unknown. Both Xiao et al. (1998) and Sekelsky et al. (1999) show that NNs contain potential for accurate retrievals of snowfall properties. Thus, a renewed investigation of NNs with the latest results from scattering models and ice particle observations (i.e., in situ and radar) is motivated.

Here, an NN for retrieving two parameters of the normalized gamma distribution (Testud et al. 2001; Delanoë et al. 2014), namely the normalized intercept parameter N_w and the mass-weighted mean diameter D_m, from radar observables and temperature is trained. Specifically, scattering results from numerous DDA and generalized multiparticle Mie method (GMM; Xu 1995) simulations of a wide variety of unrimed particle types are used in conjunction with measured particle size distributions (PSDs) from NASA field campaigns to synthesize a database of snowfall properties and their associated Z_e at GPM-DPR frequencies. This database is then used to train an NN for the simultaneous retrieval of N_w and D_m, which is evaluated against a standard power-law retrieval as well as an estimate of the current GPM-DPR retrieval. Then the NN retrieval is evaluated on coincident observations of Z_e and in situ snow properties from three case studies obtained from NASA Ground Validation campaigns. The paper is structured as follows: section 2 describes that data used in this study and how the synthetic database is generated. Section 3 contains the results of the evaluation of the retrievals on the synthetic database as well as three case studies. Section 4 discusses how the NN retrieval compares to the operational GPM-DPR algorithm and how it could be implemented on the GPM-DPR record. Section 5 summarizes the results and conclusions.

2. Data and methods

a. Description of PSD parameters

The features used for retrieving N_w and D_m within the NN are Z_e at Ku band, dual-frequency ratio ($\mathrm{DFR}_{\mathrm{Ku-Ka}}$), and temperature ($T$). Using in situ aircraft observations of PSDs sorted into different bin sizes, Z_e can be calculated by

$$Z_{e,\lambda} = \frac{\lambda^4}{\pi^5 |K|^2} \sum_{i=0}^{n_{\text{bins}}} \sigma_{\text{bsc}}(D_i, \lambda) N(D_i) \Delta D_i, \tag{2}$$

where λ is the radar wavelength, $|K|^2$ is the dielectric factor (0.93 and 0.92 for Ku and Ka band, respectively), $\sigma_{\text{bsc}}(D_i, \lambda)$ is the backscatter cross section, and $N(D_i)$ is the number distribution function for particles with maximum dimension of D_i. The i subscript indicates the ith bin of the PSD, and ΔD_i is the bin width of the ith bin. The $\text{DFR}_{\text{Ku–Ka}}$ is defined as the ratio of Z_e at Ku band ($Z_{e,\text{Ku}}$) to Z_e at Ka band ($Z_{e,\text{Ka}}$):

$$\text{DFR}_{\text{Ku–Ka}} = 10 \log_{10} \left(\frac{Z_{e,\text{Ku}}}{Z_{e,\text{Ka}}} \right). \tag{3}$$

The output targets for the retrieval are adapted versions of the three-parameter normalized gamma distribution (Testud et al. 2001; Delanoë et al. 2014). Specifically, the solid-phase mass-weighted mean diameter D_{m_s}, the liquid equivalent mass-weighted mean diameter D_{m_l}, and the liquid equivalent normalized intercept parameter N_{w_l}. Adapted versions of the normalized gamma distribution are used to supply consistency with the current GPM-DPR retrieval that outputs D_{m_l} and N_{w_l}. The D_{m_s} is defined as

$$D_{m_s} = \frac{\sum_{i=0}^{n_{\text{bins}}} m(D_i) D_i N(D_i) \Delta D_i}{\sum_{i=0}^{n_{\text{bins}}} m(D_i) N(D_i) \Delta D_i}, \tag{4}$$

where $m(D_i)$ is the mass of a particle with maximum dimension D_i. The actual assumption of the mass of each particle is discussed more in sections 2e and 2g. To calculate D_{m_l}, the liquid equivalent dimension D_{melted} must be known, and for the ith bin it is defined as

$$D_{\text{melted}_i} = \left[\frac{6 m(D_i)}{\pi \rho_l} \right]^{1/3}, \tag{5}$$

where ρ_l is the density of liquid water. Then D_{m_l} is defined as

$$D_{m_l} = \frac{\sum_{i=0}^{n_{\text{bins}}} m(D_i) D_{\text{melted}_i} N(D_i) \Delta D_i}{\sum_{i=0}^{n_{\text{bins}}} m(D_i) N(D_i) \Delta D_i}. \tag{6}$$

Chase et al. (2020) provides more details and justification for Eq. (6). The liquid equivalent normalized intercept parameter is defined following Delanoë et al. (2014), except using the D_{melted_i} rather than D_i, expressed as

$$N_{w_l} = \frac{4^4}{6} \frac{\left[\sum_{i=0}^{n_{\text{bins}}} D^3_{\text{melted}_i} N(D_i) \Delta D_i \right]^5}{\left[\sum_{i=0}^{n_{\text{bins}}} D^4_{\text{melted}_i} N(D_i) \Delta D_i \right]^4}. \tag{7}$$

Ice water content (IWC) can then be calculated from D_{m_l} and N_{w_l} by

$$\text{IWC} = \frac{N_{w_l} D^4_{m_l} \rho_l \pi}{4^4}. \tag{8}$$

The retrieval of S was not performed herein because of the added uncertainty from the myriad of particle terminal fall velocities associated with snowfall, but one could calculate S with the retrieved D_{m_l} and N_{w_l}, assuming a value for μ [shape parameter in the three-paramater gamma distribution; Borque et al. (2019) provides the guidance on the distribution of μ from the GPM Cold Season Precipitation Experiment (GCPEX)] and assuming values for the terminal fall velocity as a function of D_i. Furthermore, there is no current method to observe S from an airborne platform, which is the primary evaluation method used here.

b. DDA-GMM database

The results of numerous investigations of snowfall scattering of unrimed crystals at microwave wavelengths (Leinonen and Moisseev 2015; Leinonen and Szyrmer 2015; Lu et al. 2016; Kuo et al. 2016; Eriksson et al. 2018) are combined into a single database. Particle habits within these studies include pristine monomer shapes that occur in the atmosphere such as bullet rosettes, dendrites, plates, columns, and different aggregates consisting of these habits. The range of D_i within the combined dataset is from 13 μm to 6.3 cm. The dependence of σ_{bsc} on mass m for the Ku and Ka bands and the dependence of m on D_i for all particles used in the database are shown in Figs. 1a–c, respectively. Interestingly, even though only unrimed particles are included, a power-law fit between m and D_i to the amalgamation of all particles results in similar power-law relationship of moderately rimed particles reported in Leinonen and Szyrmer (2015) (Fig. 1c).

c. NASA GV observations

Observations collected as part of the NASA Ground Validation (GV) field campaigns (Petersen et al. 2020) were used in both the formulation of the NN and its evaluation. The formulation of the NN requires a large dataset of the three aforementioned input features (Z_e, $\text{DFR}_{\text{Ku–Ka}}$, and T), which in turn requires the use of an estimate of $N(D_i)$. In situ data collected on the University of North Dakota's Citation Aircraft (Delene et al. 2019) during the Midlatitude Continental Convective Clouds Experiment (MC3E; Jensen et al. 2016), GCPEX (Skofronick-Jackson et al. 2015) and the Olympic Mountains Experiment (OLYMPEX; Houze et al. 2017) are used here. The $N(D_i)$ is derived from measurements by two optical array probes (OAP) that capture silhouetted images of cloud and precipitation particles. In MC3E, the two-dimensional cloud probe (2DC) and the high-volume precipitation spectrometer, version 3 (HVPS3), were used for $N(D_i)$ for size ranges between 175 μm and 1 mm and between 1 mm and 3 cm, respectively. In GCPEX, the cloud imaging probe (CIP) and the HVPS3 were used, while for OLYMPEX the two-dimensional stereo probe (2DS) and the HVPS3 were used for the same size ranges as MC3E, respectively. All OAP data were processed using the University of Illinois–University of Oklahoma Optical array Probe Software (UIOOPS; McFarquhar et al. 2017; Jackson et al. 2014) to remove shattered artifacts and reconstruct both hollow images and images of particles whose edges touched one of the sides of the photodiode array. The 1-s PSDs were then averaged to 10 s to allow for better sampling statistics of large particles (McFarquhar et al. 2007) and to have similar horizontal spatial scales to that of the airborne radar.

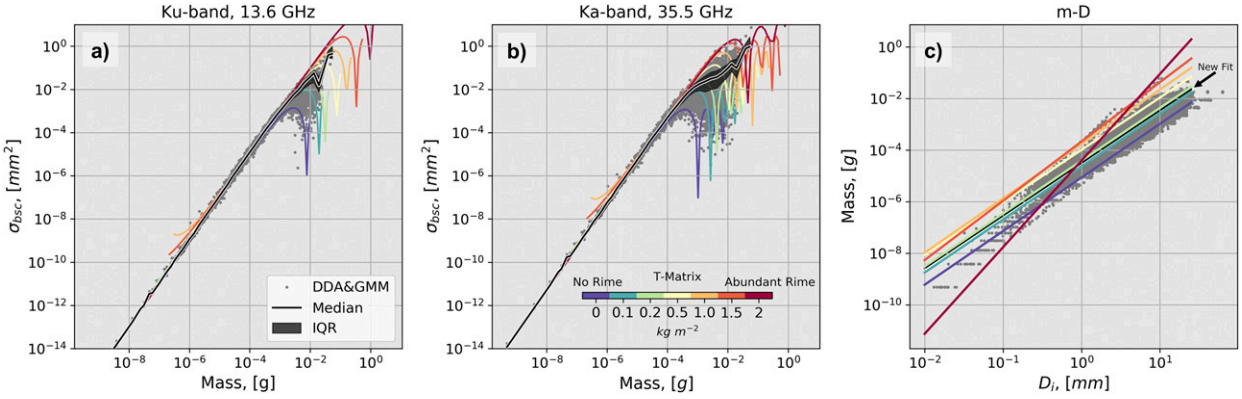

FIG. 1. Combination of all DDA/GMM particles simulated from studies mentioned in section 2b. Each dot represents an individual particle that has had its scattering properties simulated. (a) Ku-band and (b) Ka-band backscatter cross section (σ_{bsc}; dots). The IQR and median are shown in the black shading and black line, respectively. Rainbow curves are the σ_{bsc} as predicted from T matrix (Mishchenko and Travis 1998) using pyTmatrix (Leinonen 2014). The particles are oblate spheroids with axis ratios of 0.6 and 0° incidence angle with the mass predicted by the mass–dimension relations from Leinonen and Szyrmer (2015). Bluer colors indicate less riming; redder colors indicate more riming [see the color bar in (b)]. (c) The mass of all DDA/GMM particles as a function of particle maximum dimension D_i. Rainbow lines are the mass–dimension power-law fits from Leinonen and Szyrmer (2015) for various degrees of riming. The solid black line with annotation is the mass–dimension power-law fit to the DDA/GMM database of the form Eq. (9). The a and b coefficients for the new power-law fit are 0.042 and 2.04, respectively (in SI units).

To evaluate the trained retrieval, dual-frequency radar measurements collected by the Airborne Precipitation Radar (APR), versions 2 and 3, were used. The APR is a scanning radar that collects beam matched measurements of Z_e at 13.4 and 35.6 GHz (Ku and Ka band) ±25° from nadir through 24 scans (Sadowy et al. 2003; Durden et al. 2019). The nominal vertical resolution of the radar is 30 m, while the along-track resolution is approximately 1 km. The APR was flown on NASA's DC8 aircraft, which flew mostly constant altitude flight legs above precipitation echoes. The APR, version 2, was used in GCPEX and had a nominal sensitivity of 0 and −20 dBZ for the Ku band and Ka band, respectively, while the APR, version 3, was used in OLYMPEX with a sensitivity of 10 dBZ and −20 dBZ for Ku band and Ka band, respectively. The only difference between versions 2 and 3 was the addition of 94 GHz (W band) measurements in the APR, version 3. Since this work is GPM-DPR centric and attenuation from snowfall at W band is nontrivial, up to 1 dB km^{-1} whereas at Ku and Ka band are estimated to be around 0.1 dB km^{-1} or less (Kneifel et al. 2011), only the Ku- and Ka-band reflectivities are used.

To ensure correct absolute calibration of the radars, the Ku-band radar is calibrated by considering surface echoes of a water body in nonprecipitating conditions (GCPEX: Lake Huron and Lake Ontario; OLYMPEX: Pacific Ocean; Tanelli et al. 2006). Then the Ka band is calibrated against the Ku band by considering low reflectivity regions of the echoes where there is likely scattering in the Rayleigh regime (Durden et al. 2019). The uncertainty in this calibration is estimated to be approximately 1 dB for Ku and Ka band.

Several steps of processing of the APR data are required before its use in the retrieval. While attenuation from O_2 and H_2O vapor is small, they are corrected for using the gaspl package in MATLAB (Radiocommunication Sector of International Telecommunication Union 2013; https://www.itu.int/dms_pubrec/itu-r/rec/p/R-REC-P.676-10-201309-S!!PDF-E.pdf) and a thermodynamic sounding collected near the time of the radar data collection. The mean values for two-way correction from gaseous attenuation is 0.15 and 0.6 dB for Ku and Ka band, respectively at the surface. Since the focus of this analysis is on only solid-phase hydrometeors, liquid-phase echoes, melting echoes (i.e., the bright band), surface echoes, and the radar returns from the in situ aircraft itself were all removed prior to running the retrieval. Liquid-phase echoes where determined as the echoes found at altitudes lower than the melting level

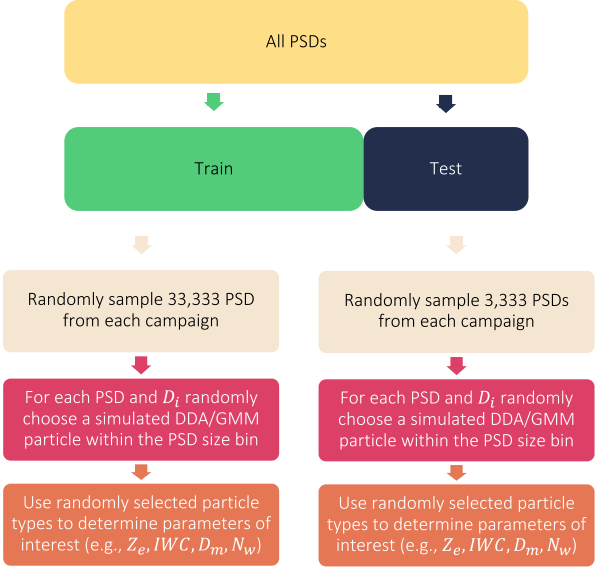

FIG. 2. Flowchart of how the database of PSD parameters used to train and evaluate the neural network is generated.

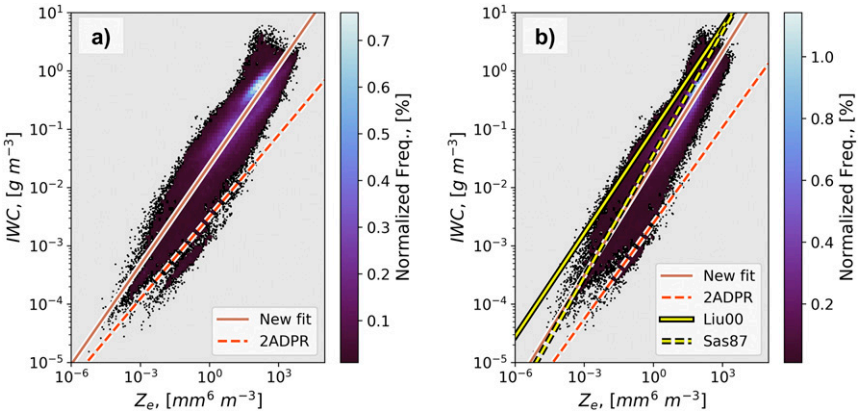

FIG. 3. Joint distributions of Z_e–IWC for the synthetic database generated from the DDA/GMM particles and measured PSDs. (a) Ku-band and (b) Ka-band results. The solid red line is the new power-law fit to the data plotted, and the dashed red line is the version-6 GPM-DPR power-law fit (see appendix A). Additional yellow lines in (b) are two power-law fits from Liu and Illingworth (2000) (solid line) and Sassen (1987) (dashed line).

that was determined by considering the peak in linear depolarization ratio (LDR). Furthermore, echoes found near or below the minimum sensitivity of the Ku-band Z_e were removed (10 and 0 dBZ for OLYMPEX and GCPEX, respectively).

To execute the NN retrieval, a T profile is required. For the APR, the T and altitude measured by the University of North Dakota (UND) Citation are used from each mission day to construct a mean temperature profile. This profile is then linearly interpolated to the APR vertical resolution. The Citation T is used as opposed to a radiosonde observation because it flew in a region more representative temporally and spatially of the environment sampled by the radar. A sensitivity test using the observed sounding as opposed to the Citation derived sounding resulted in an absolute mean percent difference of 5%, 20%, and 14% for D_{ml}, N_{w_l}, and IWC, respectively.

d. Collocation of in situ and radar measurements

To quantitatively evaluate the output of the NN retrieval, collocated in situ and radar data are required. Collocated points are identified following a technique similar to Chase et al. (2018) and Ding et al. (2020), who used a kd-tree searching algorithm from Scipy (Oliphant 2007) to efficiently search the APR sample volume for 30 of the closest gates within 1 km of the in situ aircraft location. One difference from Chase et al. (2018), where the weighted mean of the 30 closest gates were used, is that the closest gate is chosen from the 30 closest located by the kd-tree algorithm. The closest gate method was chosen to prevent auto correlations in the radar data from influencing the performance statistics. Testing the sensitivity between the 30-gate average used in Chase et al. (2018) and the closest gate used here results in a Z_e change of less than the calibration uncertainty (<1 dB). The average spatial error of collocation is approximately 370 m. Another difference from Chase et al. (2018) is that observations were considered coincident for this study when they were collected within 5 min temporally, while Chase et al. (2018) used a 10-min temporal threshold.

e. PSD parameter reference from in situ

While an independent measure of bulk water content within clouds was made during GCPEX and OLYMPEX, previous studies have suggested the Nevzorov probe, used in both field campaigns, underestimates mass in comparison with other bulk water content probes (e.g., Korolev et al. 2013; Abel et al. 2014). Since an estimate of particle mass is required to calculate D_{m_l}, D_{m_s}, N_{w_l}, and IWC, a parameterization given by

$$m = aD^b \tag{9}$$

is used, where a and b can vary depending on the conditions where the measurements were obtained or on the probes used to collect the data (Finlon et al. 2019). To constrain the choice of a and b, the collocated Z_e from the APR and the Z_e calculated from the PSD are compared. Specifically, Z_e is calculated from the PSD using Eq. (2) and the σ_{bsc} from 6 different degrees of riming categories reported in Leinonen and Szyrmer (2015). Then, the a and b parameters associated with the σ_{bsc} that provides least error between measured and calculated Z_e at both Ku and Ka band are chosen. From there, D_{m_l}, D_{m_s}, N_{w_l}, and IWC are all calculated using the selected a and b.

TABLE 1. RMSE of the retrieved IWC (g m^{-3}) using the power-law fits on the synthetic test dataset. Sassen (1987) and Liu and Illingworth (2000) only had Ka-band fits. For convenience, the α and β parameters of each of the power laws are included in the table. Ku-band parameters are in parentheses, and Ka-band parameters are in square brackets.

	Ku band	Ka band	(α_{ku}, β_{ku}); [α_{ka}, β_{ka}]
DDA/GMM	0.29	0.25	(0.024, 0.570); [0.026, 0.638]
2ADPR	0.47	0.47	(0.003, 0.469); [0.002, 0.548]
Sassen (1987)	—	0.53	(—, —); [0.037, 0.7]
Liu and Illingworth (2000)	—	0.87	(—, —); [0.097, 0.59]

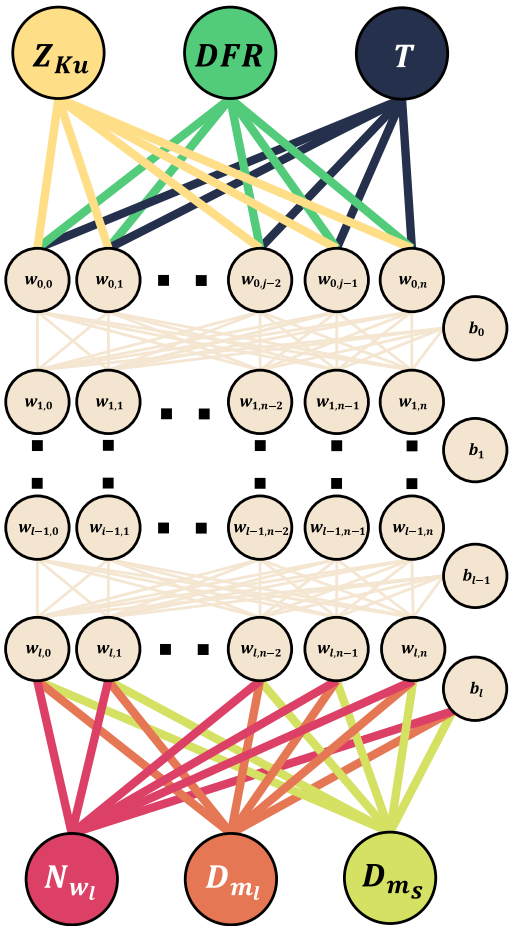

FIG. 4. Neural network architecture; see Table 2 for more detail. Input parameters are Z_{ku}, DFR and temperature T. Outputs are N_{w_l}, D_{m_l}, and D_{m_s}. There are six hidden layers, with weights $w_{i,j}$, where i and j are the layer and neuron number, respectively. The bias parameters are labeled as b_i. Activation functions are all the same but are not shown here to save space.

The average error of Z_e from this method is 0.20 and 1.3 dB for Ku and Ka band, respectively.

f. GPM-DPR observations

The current GPM-DPR retrieval process is described in the algorithm theoretical basis document (Iguchi et al. 2018). To compare the current GPM-DPR retrieval of N_{w_l} and D_{m_l} to the NN retrieval developed herein, the NN retrieval is applied directly to the GPM-DPR data, which are the version-6 level-2 (2ADPR) data product. As with the APR data, an estimate of T at each radar gate is required. Thus, to allow for consistency between the NN retrieval and the GPM-DPR retrieval, the NN when applied to the GPM-DPR data uses the same T data used in the GPM-DPR algorithm that are provided by the Japan Meteorological Agency numerical weather prediction model.

g. Snowfall properties database

The process of creating the training and test dataset for the NN is described here and is shown graphically in Fig. 2. The

TABLE 2. Specific parameters used to train the neural network.

Software	Tensorflow
No. of hidden layers	6
No. of neurons per layer	8
Optimizer	RMSprop
Activation function	Rectified linear unit (ReLU)
Initial learning rate	0.001
Input shape	3
Output shape	3
Batch size	128
Loss function	Mean square error
No. of epochs	125

PSD dataset is split into training and testing groups by randomly selecting 333 PSDs (approximately 10% of the PSD data) without replacement from each field campaign and labeling them as the test dataset. The remaining 15 487 PSDs are labeled as the training dataset. Then the datasets are upscaled by randomly sampling with replacement. For the training dataset, 33 333 PSDs from each campaign are randomly sampled, whereas for the test dataset 3333 PSDs are sampled, providing a 90%/10% split between the two datasets. For each bin characterizing a PSD, one DDA-GMM particle is randomly sampled with replacement that has a maximum dimension D_p such that $D_i - (\Delta D_i/2) \leq D_p \leq D_i + (\Delta D_i/2)$. This creates a random distribution of simulated particle types that match the prescribed dimensions of D_i and subsequently $N(D_i)$. Once a random collection of particles is assigned to each PSD, Z_e,D_{m_l},N_{w_l}, and IWC are calculated using the particle type information provided by the DDA-GMM simulations and the equations shown in section 2a. Note that, although there is no additional information gained from upscaling the PSD data, there are over 20 000 particles that create numerous unique combinations of particles and PSDs. The unique combinations provide a wider variety of plausible microphysical/microwave properties, which should allow the NN to become more generalized.

To provide context of Z_e and IWC that have been synthetically generated, the joint distribution of Z_e and IWC is shown in Fig. 3. Additional information of the range of different radar scattering properties of the training database can be found in appendix B and Fig. B1. It is not surprising that the range of IWC calculated is larger than that measured by the bulk water probes used in MC3E, OLYMPEX and GCPEX (e.g., Nevzorov) because the probes are known to underestimate IWC. Thus, the data are kept for training in order to provide a spectrum of plausible values to the NN.

A new power law between Z_e and IWC (solid red line in Fig. 3) of the form

$$\text{IWC} = \alpha Z_e^{\beta} \tag{10}$$

was obtained from the training dataset, and the coefficients are listed in Table 1. This relationship provides a baseline retrieval to compare with the NN. Herein this will be referred to as the legacy method retrieval. A comparison of the new legacy method with previous relations (e.g., Sassen 1987; Liu and Illingworth 2000) shows that the new fit generally estimates lower IWC for the same Z_e by approximately 300% and 50%

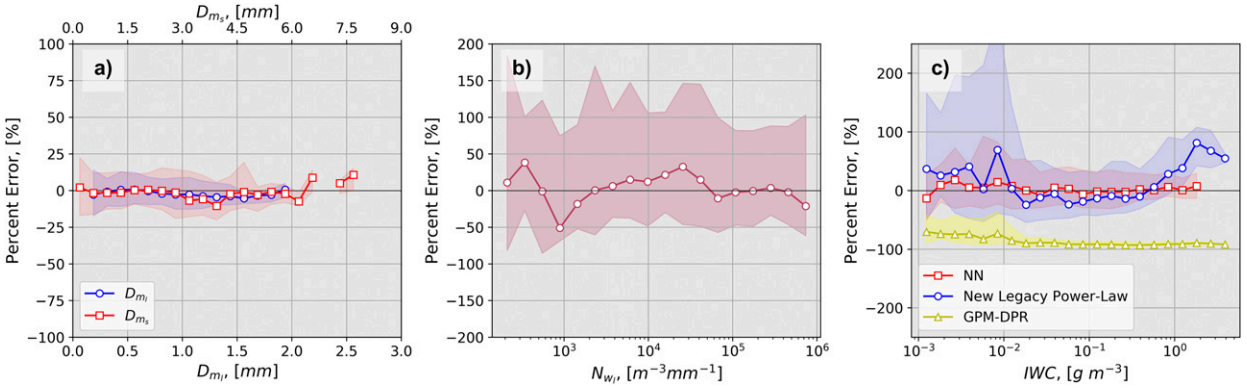

FIG. 5. Percent error as a function of retrieved parameter magnitude. (a) Median error associated with D_{m_l} (solid blue line circle markers; bottom x axis) and with D_{m_s} (solid red line square markers; top x axis). The interquartile range is shown in shading. (b) As in (a), but for N_{w_l}. (c) As in (a) and (b), but for IWC. The red shading and line are from the neural network, the yellow shading and line are from the average Ku-band GPM-DPR relation, and the blue shading and line are for the Ku-band legacy power-law relation trained on the synthetic database.

relative to the Liu and Illingworth (2000) and Sassen (1987) relations, respectively. For a second comparison, an average relation of the form in Eq. (10) is obtained from output of the current GPM-DPR algorithm (see appendix A). The IWC obtained from the GPM-DPR relation are approximately a factor of 10 smaller than the IWC generated here. Since S is proportional to IWC, it is consistent with Skofronick-Jackson et al.'s (2019) study showing that GPM-DPR is underestimating S. To quantify the error in retrieved IWC for all retrievals, the root-mean-square error (RMSE),

$$\mathrm{RMSE} = \sqrt{\frac{\sum_{0}^{n}(x_r - x_t)^2}{n}} \tag{11}$$

is used, where x_r is the vector of retrieved values, x_t is the vector of true values, and n is the number of data samples in the test set. The RMSE for each legacy method calculated on the test dataset is shown in Table 1.

h. NN details

The type of NN used here is a fully connected feed forward multilayered perceptron NN. The network has three input features, six hidden layers of eight neurons and three output labels (Fig. 4). The input features were chosen based on what is available operationally from GPM-DPR, namely the Ku-band Z_e in logarithmic units (dBZ), the $\mathrm{DFR}_{\mathrm{Ku-Ka}}$ in logarithmic units (dB) and the T in degrees Celsius. The structure of the network was determined by systematically retraining the network with 2–128 neurons and 2–10 layers and choosing the network with the least amount of error on the test dataset before showing a signal of overfitting. All networks were trained on graphical processing units (GPUs) provided by Google's freely available computation platform (Google Colaboratory) and the open source software package Tensorflow (Abadi et al. 2016).

Before training, the data require a transformation to prevent weighting any specific input feature unfairly based on its absolute magnitude and range. Thus, all input features were scaled to have a mean of 0 and a variance of 1. In addition, taking the logarithm of the output labels and scaling them to have mean 0 and variance of 1 provided the least RMSE. All parameters described above, as well as a few other specific details, are noted in Table 2. In the event the reader would like to use the trained NN, an example of loading and running the network is shown in a Jupyter notebook with the associated data included with this paper (see data availability statement).

3. Results

a. Evaluation of the retrieval methods on the synthetic dataset

Any empirical method can be overfit intentionally to provide optimal results on a training dataset. Thus, here the NN retrieval is evaluated on the test dataset. The median percent error (MPE), defined as

$$\mathrm{MPE} = \mathrm{median}\left(100 \times \frac{y_r - y_t}{y_t}\right), \tag{12}$$

where y_r is the vector of retrieved values and y_t is the vector of true values, is chosen as the metric of evaluation. Figure 5 shows the MPE as a function of the retrieved parameter of interest's magnitude. For retrieved D_{m_l} and D_{m_s} there is little bias, with MPE around 0% and an interquartile range (IQR) on average of ±17% and ±23% for D_{m_l} and D_{m_s}, respectively (Fig. 5a). Similarly, N_{w_l} has MPE of 2% but has much larger

TABLE 3. RMSE of snowfall parameter retrieved by the NN on the synthetic test dataset.

Parameter	RMSE
D_{m_l} (D_{m_s})	0.12 (0.41) mm
N_{w_l}	1.27×10^6 $\mathrm{m^{-3}\,mm^{-1}}$
IWC	0.24 $\mathrm{g\,m^{-3}}$

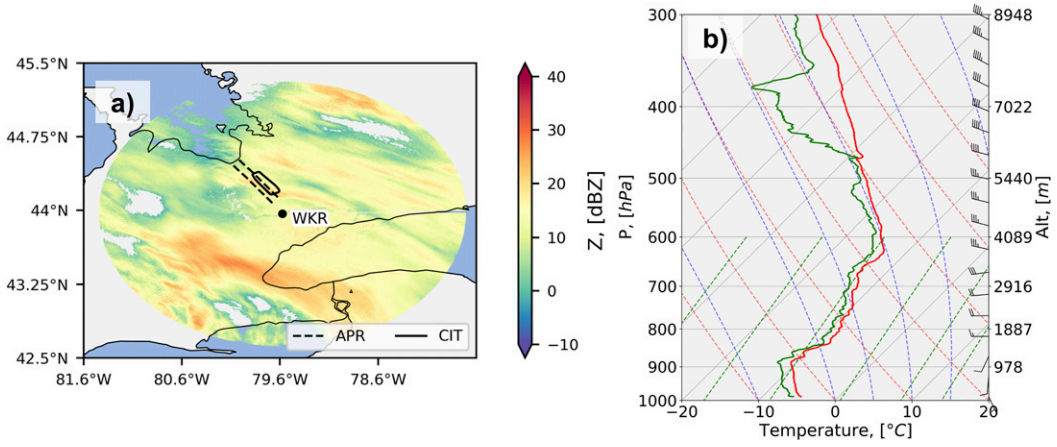

FIG. 6. (a) Map with of GCPEX domain with a PPI from the Environment and Climate Change Canada's C-band radar located at King City, Ontario (WKR), at 0015 UTC 31 Jan 2012. The solid black line is the Citation aircraft track, and dashed black lines are the extent of the APR-2 scan volume at the ground. (b) Radiosonde observation taken at 2218 UTC 30 Jan 2012 at the WKR site. One full wind barb indicates 10 m s^{-1}.

average IQR than does D_m, with the mean first quartile being −51% and the mean third quartile being +114%.

Using Eq. (8), IWC can be calculated so that the NN retrieval can be compared directly to the legacy methods. The NN (red in Fig. 5c) performs best, showing a MPE around +1%, and a mean first quartile of −25% and a mean third quartile of +43%. As the magnitude of the retrieved IWC increases, the IQR decreases, implying that there is less relative uncertainty when the retrieval is retrieving IWC $\geq$ 0.5 g m^{-3}. Meanwhile, the legacy fit provided in section 2g (blue in Fig. 5c) provides the second-best method. There is a clear high bias of +35% at IWC $\leq$ 0.01 g m^{-3} and of +61% IWC $\geq$ 1.0 g m^{-3}, while underestimating between 0.01 g m^{-3} < IWC < 1.0 g m^{-3}. The legacy fit also shows considerably more uncertainty than the NN, showing a larger IQR. The estimation of the current GPM-DPR algorithm (yellow in Fig. 5c) shows a constant underestimation for all IWC of approximately 86%.

Comparing the RMSE of the NN retrieved IWC (Table 3) with the RMSE of the legacy methods (Table 1), the NN

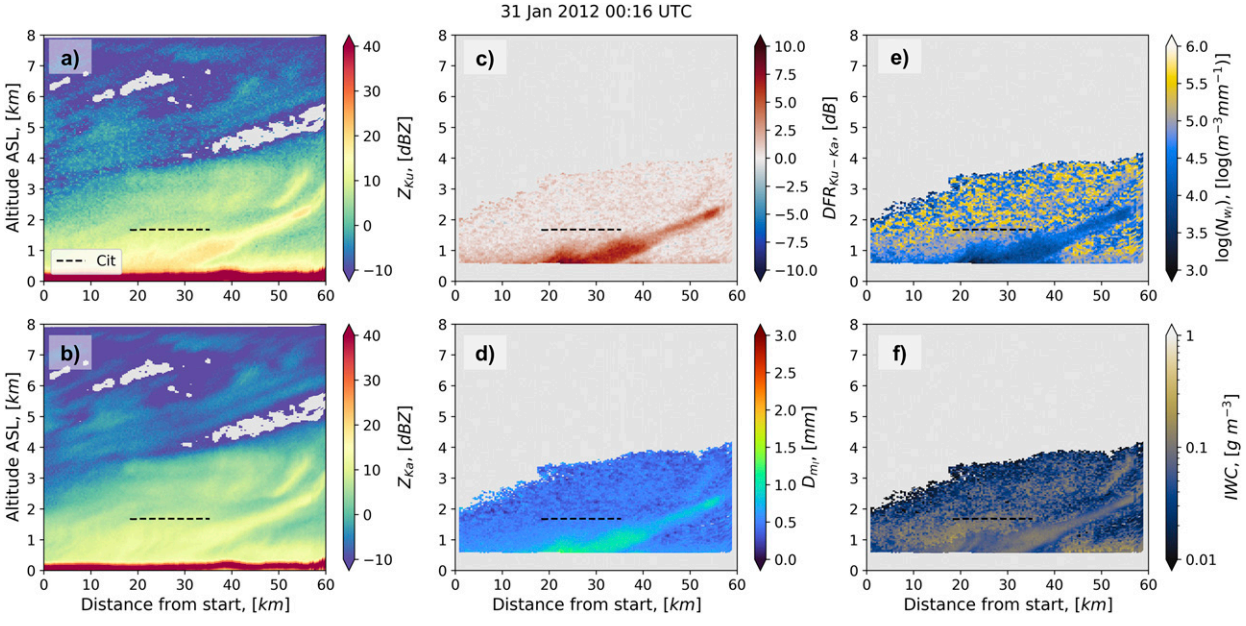

FIG. 7. Cross section at near nadir from the APR-2 along the flight shown in Fig. 6. (a) Observed Z_{Ku}. The Citation flight track within ±5 mins of radar data collection is shown with the dashed black line. (b) Observed Z_{Ka}. (c) Dual-frequency ratio between Ku and Ka band (DFR_{Ku-Ka}). Echoes are filtered to remove melting particles, surface returns, rain echoes, noise above echo top, and the Citation aircraft echo itself. (d) Retrieved D_{m_l} using the neural network. (e) Retrieved N_{w_l} using the neural network (f) Calculated IWC from the retrieved D_{m_l} and N_{w_l} using the neural network.

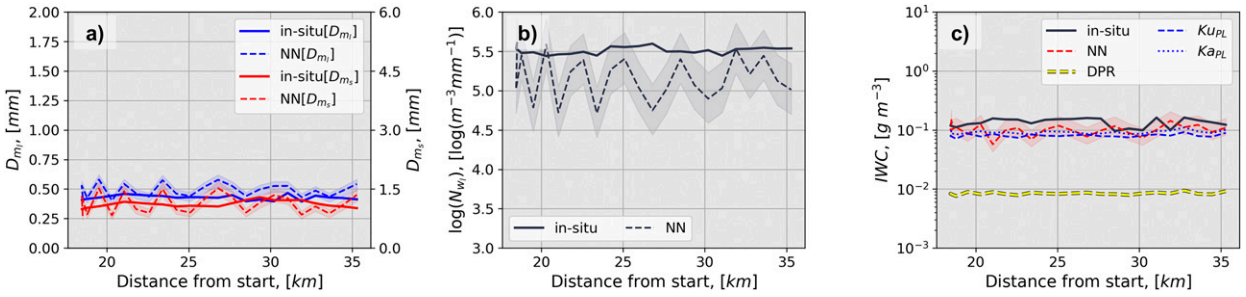

FIG. 8. Along-track comparison between in situ measurements and collocated retrieved products for 31 Jan 2012. (a) Solid lines indicate the best estimate of D_{m_l} (blue) and D_{m_s} (red) calculated from PSD; matched neural network retrievals of D_{m_l} (blue) and D_{m_s} (red) are dashed lines. (b) Similarly, best estimate of N_{w_l} is the solid line calculated from PSD; the matched neural network retrieval is the dashed line. (c) Best estimate of IWC is the solid black line; the matched neural network retrieval is the dashed red line (NN). The average power-law relation for current GPM-DPR algorithm (DPR; yellow dashed) and new power-law fits for Ku (Ku_{PL}; blue dashed) and Ka band (Ka_{PL}; blue dotted) are shown for reference.

outperforms all other legacy methods. To test statistical significance, a two-sample Student's t test is used to compare the square error of the legacy methods to the square error of the NN retrieval. The result shows that the NN has a significantly ($p < 0.05$) lower square error than all methods except the Ka-band legacy power-law fit. Thus, the NN retrieval provides estimates of IWC that are equal to or better than legacy method, while additionally retrieving two parameters of the PSD.

b. Case studies

While the evaluation of the NN on the test dataset provides an initial quantification of uncertainty and errors, the test dataset may not be truly independent from the training dataset. The PSDs used to synthesize the training and test dataset were measured in close spatial and temporal proximity to each other and thus are potentially correlated. The aforementioned implicit correlation could have skewed the evaluation done in section 3a. Furthermore, the stochastic nature of particle selection in the synthetic database could be unphysical, leading to training and evaluation of the NN on potentially unphysical Z_e, D_{m_l}, and N_{w_l} triplets. Thus, to gain more confidence in the NN retrieval and more physical insight, three case studies are used to further evaluate the retrieval.

1) 31 JANUARY 2012

The first case study is a synoptic snowfall event from GCPEX that occurred on 31 January 2012 (Fig. 6). This case represents a typical continental cyclone, with warm air advection leading to widespread light snowfall over the GCPEX domain. Both aircraft flew a coordinated flight around 0016 UTC with the Citation flying an oval pattern northwest of the King City (Ontario, Canada) radar and the DC-8, carrying the APR, flying straight overtop the Citation (Fig. 6a). The sounding from the start of the mission (2218 UTC 30 January 2012) shows temperatures from the surface to 750 hPa are between −5° and −10°C, with the dendritic growth zone located between 700 and 600 hPa (Fig. 6b). The King City ground-based C-band radar plan position indicator (PPI) scan shows widespread snow, with localized bands of higher Z_e (Fig. 6a).

Considering the cross section at near nadir of the swath shown in Fig. 6a, meteorological radar echoes are found up to the altitude of the DC-8 (8 km; Fig. 7a). However, echoes that are sufficiently above the minimum sensitivity of Ku-band radar only extend to 4 km. A clear fall-streak echo pattern shows up in the Ku and Ka band as well as the $DFR_{Ku–Ka}$ (Fig. 7c) between 20 and 60 km horizontally and between 0 and 3 km vertically. The results of applying the NN retrieval to the APR data are shown in Figs. 7d–f. Only D_{m_l} is shown because D_{m_s} is highly correlated to D_{m_l}. Within the fall streak, D_{m_l} is 0.75–1.00 mm, while outside the fall streak it is $\leq$ 0.5 mm (Fig. 7d) consistent with the increase in particle size in fall streaks noted by Plummer et al. (2015). Inversely, N_{w_l} within the fall streak is lower than the surrounding cloud (Fig. 7e). Calculating IWC shows peak values found within the fall streak of approximately 0.1 g m^{-3}.

The retrieval data matched to the in situ plane are shown in Fig. 8. Both the retrieval and in situ measurements of D_{m_l} have good agreement showing an MPE of less than 15%. The retrieval of N_{w_l} performs worse than that of the D_{m_l}, showing a constant low bias of approximately 0.5 in units of log(m^{-3} mm^{-1}). This low bias propagates into the calculation of IWC that is biased low

TABLE 4. RMSE and MPE (in parentheses) from the 31 Jan 2012 case study. Asterisks indicate that the exponential relations do not explicitly predict any other parameter except IWC.

Parameter	NN	DDA/GMM Ku, Ka	2ADPR
D_{m_l}, D_{m_s}	0.08, 0.25 mm; (+11%, −7%)	*	*
N_{w_l}	1.87×10^5 m^{-3} mm^{-1}; (−61%)	*	*
IWC	0.05 g m^{-3}; (−28%)	0.06, 0.05 g m^{-3}; (−43%, −34%)	0.13 g m^{-3}; (−94%)

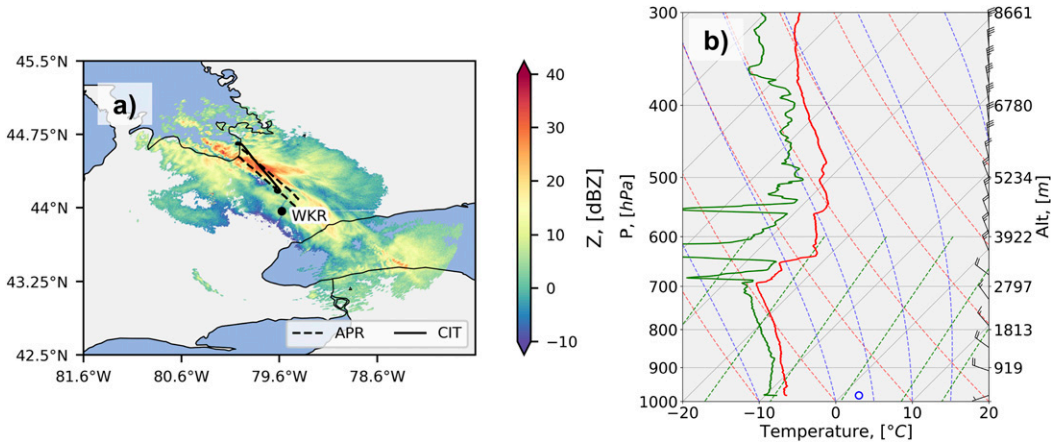

FIG. 9. As in Fig. 6, but for 12 Feb 2012. (b) Radiosonde observation taken at 0640 12 Feb 2012, with the blue open circle near 1000 hPa indicating average surface temperature of Lake Huron from the National Oceanic and Atmospheric Administration CoastWatch Great Lakes.

by approximately 0.05 g m^{-3}. The RMSE and MPE between the retrieved parameters and the in situ estimates are found in Table 4. For this relatively uniform low IWC case, the NN retrieval performs better than suggested in Table 3.

2) 12 FEBRUARY 2012

The second case analyzed evaluates the NN retrieval on a shallow convective snowfall event (i.e., lake effect snow) from 12 February 2012 during GCPEX. The PPI scans from the King City radar show a narrow band of snowfall emanating from Georgian Bay and impacting the local Southern Ontario region (Fig. 9a). A radiosonde observation taken 40 min after the flights in Fig. 9b, show cold 850 hPa temperatures at about −15°C providing ample conditional instability for lake-effect snow given an average lake surface temperature of Lake Huron of 2°C. The DC-8 and Citation flew multiple legs between Georgian Bay and the King City radar site, transecting the lake effect snowbands.

The cross section shown from 12 February 2012 shows echo tops much shallower than 31 January 2012, peaking at approximately 2.5–3 km MSL (Fig. 10). Individual convective elements are seen in the Z_e field, diagnosed from the pockets of $Z_e \geq 30$ dBZ (Fig. 10a), which contained observed Doppler velocities of 1.0–1.5 m s^{-1} upward (not shown). There are no clear fall streaks in this case, but DFR$_{\mathrm{Ku–Ka}}$ is locally increased to >5 dB at 40–60 km (Fig. 10c). The retrieved D_{m_i} is increased in the larger DFR$_{\mathrm{Ku–Ka}}$ regions to 1–1.5 mm (Fig. 10d) while being near 0.5 mm outside. The same larger DFR$_{\mathrm{Ku–Ka}}$ regions

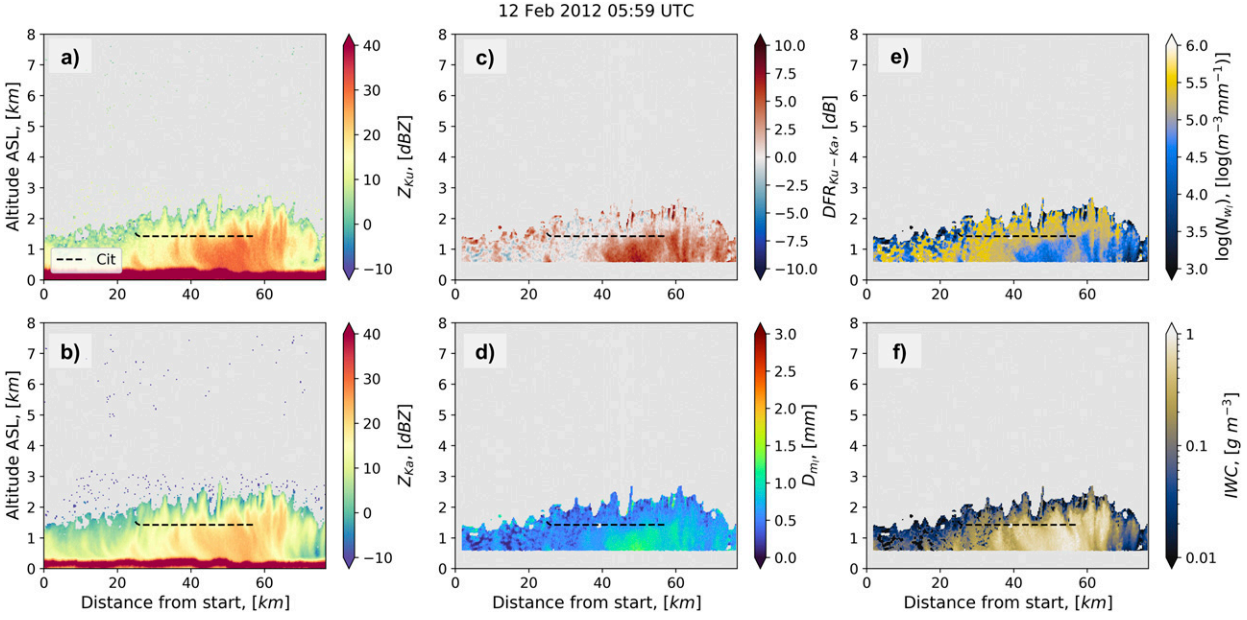

FIG. 10. As in Fig. 7, but for 12 Feb 2012.

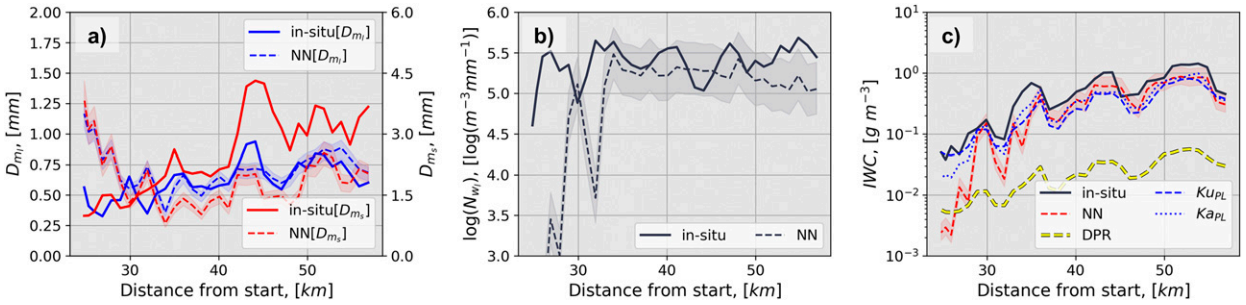

FIG. 11. As in Fig. 8, but for 12 Feb 2012.

are characteristic of N_{w_l} around 3.5 log(m^{-3} mm^{-1}) and IWC around 1 g m^{-3}.

In comparing the retrieved D_{m_l} with in situ data, it is seen that there is an initial poor agreement that appears along the flight track, with the retrieval overestimating the measured values by 0.75 mm, but then agreement improves along the track by 35 km (Fig. 11a). This could be due to the poor temporal matchup between the APR and the Citation (5 mins at the start) and the large spatial heterogeneity. Interestingly, unlike the previous case where the performance of the retrieved D_{m_s} was similar to the performance of the D_{m_l}, retrieved D_{m_s} shows a constant low bias of a factor of 2 (Fig. 11a) at the same location where the retrieval of D_{m_l} is performing well (with MPE of 8%). The retrievals of N_{w_l} and IWC show the same poor agreement at the start, but then agree within 33%–43% (MPE) at distances greater than 35 km. Although the N_{w_l} retrieval has less error (by 13%) relative to the 31 January 2012 case, the retrieval of IWC is still low when compared with the in situ measurement but is performing better than the other legacy methods. The retrieved RMSE of parameters for 12 February 2012 are worse than the RMSE on the synthetic data and the previous case, but the NN retrieval outperforms all legacy methods in retrieving IWC with a RMSE of 0.27 g m^{-3} (Table 5). It should be noted that during the 12 February 2012 case, the Citation was detecting the presence of supercooled liquid water from the Rosemount icing detector probe (Baumgardner and Rodi 1989), which implies that rimed particle types are plausible and could partially explain why the retrieval performs worse on the 12 February 2012 case than the 31 January 2012 case and the synthetic dataset.

3) 3 DECEMBER 2015

The last case presented herein considers a synoptically forced event that occurred over complex topography on 3 December 2015 during OLYMPEX. The 1.45° PPI scan from the National Weather Service Langley Hill (Washington) S-band radar shows widespread precipitation echoes, with enhancements of reflectivity over the terrain located NE of the radar location (Fig. 12a). A radiosonde from approximately the same time and location as the ground-based radar scan shows a moist environment, with the melting level located at approximately 750 hPa (or 2 km MSL). Both airplanes were flying a coordinated stacked leg pattern from northwest to southeast over the Olympic Mountains (dashed and solid line in Fig. 12a).

The cross section of raw Z_e and the retrieved products are shown in Fig. 13. Echo tops at Ku and Ka band on 3 December 2015 extend up to about 8 km MSL, with an apparent melting level at 2 km (i.e., bright band; Figs. 13a,b). Interestingly, there is also a secondary level of enhancement of Z_e found at 3.5–4.5 km that shows up well in $DFR_{Ku–Ka}$ (Fig. 13c). The secondary enhancement is characteristic of larger retrieved D_{m_l}, lower N_{w_l}, and larger IWC than the immediate surrounding areas. This region of enhancement is likely associated with a mountain wave, forced by a stable layer lifted by synoptic flow over the terrain, leading to locally increased upward vertical velocities within the layer. Doppler velocities within the second layer of enhancement showed pockets of 1–2 m s^{-1} updrafts (not shown). Considering the in situ measured temperature and the sounding (Fig. 12b), the secondary enhancement is close to the dendritic growth zone, which could be leading to quickly growing particles by vapor deposition and aggregation and thus the enhanced Z_e and $DFR_{Ku–Ka}$. Below the layer of enhancement, retrieved IWC increases above 1 g m^{-3}.

There is good agreement between the retrieval and in situ observations initially, with MPE of −8%, +9%, and −8% for D_{m_l}, N_{w_l}, and IWC, respectively, up to 65 km. After 65 km, the retrieval underestimates D_{m_l} and D_{m_s} (−17% and −28% MPE, respectively; Fig. 14a), and overestimates N_{w_l} (+163% MPE; Fig. 14b) leading to an overestimate of IWC (+31% MPE; Fig. 14c). The RMSE of all parameters shows less error than 12 February 2012,

TABLE 5. As in Table 4, but for the 12 Feb 2012 case study.

Parameter	NN	DDA/GMM Ku, Ka	2ADPR
D_{m_l}, D_{m_s}	0.25, 1.44 mm; (+8%, −34%)	*	*
N_{w_l}	1.79×10^5 m^{-3} mm^{-1}; (−48%)	*	*
IWC	0.27 g m^{-3}; (−38%)	0.33, 0.29 g m^{-3}; (−42%, −37%)	0.67 g m^{-3}; (−96%)

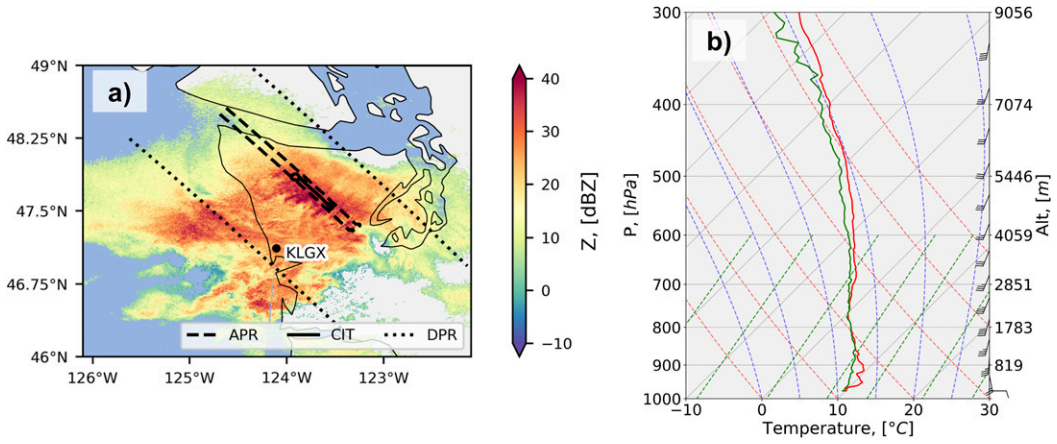

FIG. 12. As in Fig. 6, but for 1509 UTC 3 Dec 2015 and the Langley Hill NEXRAD radar (KLGX). (a) A second set of lines (dotted) indicates the GPM-DPR inner swath where Ku- and Ka-band observations are made. (b) Radiosonde observation taken at 1516 UTC 3 Dec 2015 from near the marked radar location in (a).

but larger errors than the case on 31 January 2012 (Table 6). As in the 12 February 2012 case, there is supercooled liquid water sampled by the Citation aircraft on 3 December 2015, which was noted by Chase et al. (2018) and could be leading to the observed errors in the NN retrieval. Despite the potential presence of rimed particles, the retrieval of IWC shows similar RMSE (0.16 g m^{-3}) to the legacy methods (0.22 and 0.17 g m^{-3}) and improved results relative to GPM-DPR average relation (0.42 g m^{-3}).

4) SUMMARY OF CASES

Three case studies representing different meteorological conditions were analyzed to compare the retrieved D_{m_l}, D_{m_s}, N_{w_l}, and IWC with the in situ measured value. Combining all three, the case studies show that the NN performs similarly to what was described in section 3a (Table 3), with statistically significant ($p < 0.05$) lower square error on IWC when compared with an estimate of the current GPM-DPR algorithm and a legacy power-law fit using Ku-band Z_e. The resulting combined MPE is −13%, −23%, +120%, and +10% for D_{m_l}, D_{m_s}, N_{w_l}, and IWC, respectively. It is important to emphasize that for cases 2 and 3 the NN is performing better than legacy methods despite the presence of potentially rimed particles being sampled in situ. Thus, while the formulation of the training dataset is somewhat simple (i.e., no rimed particles), it is still general enough to provide improved retrieval results

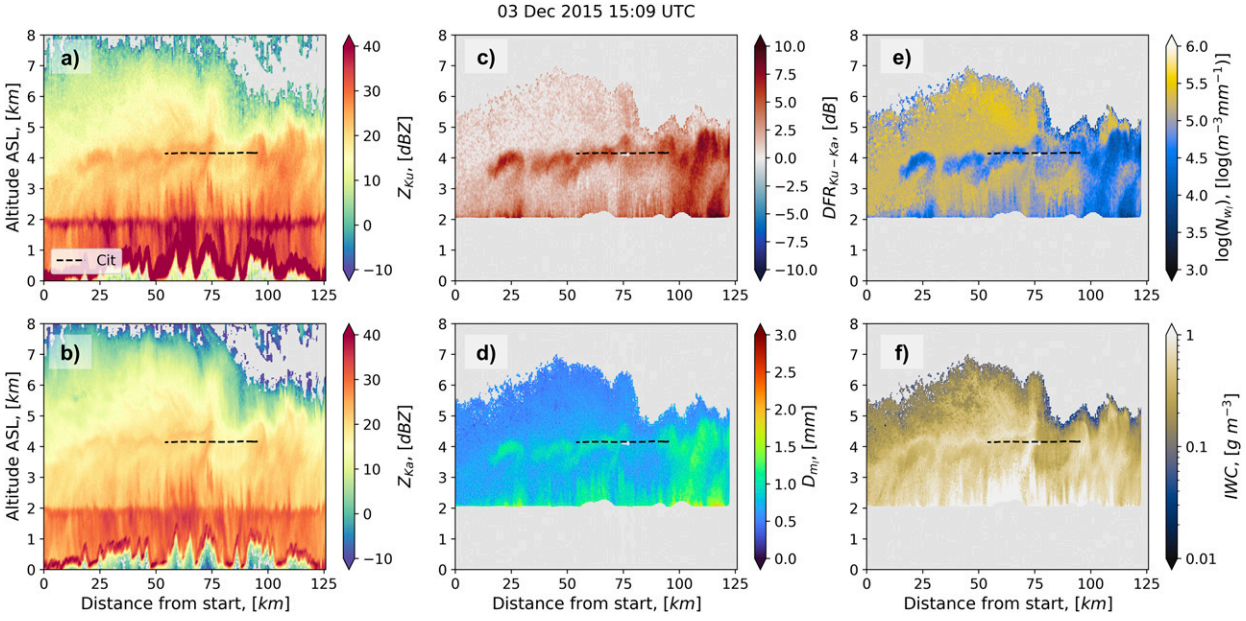

FIG. 13. As in Fig. 7, but for 3 Dec 2015.

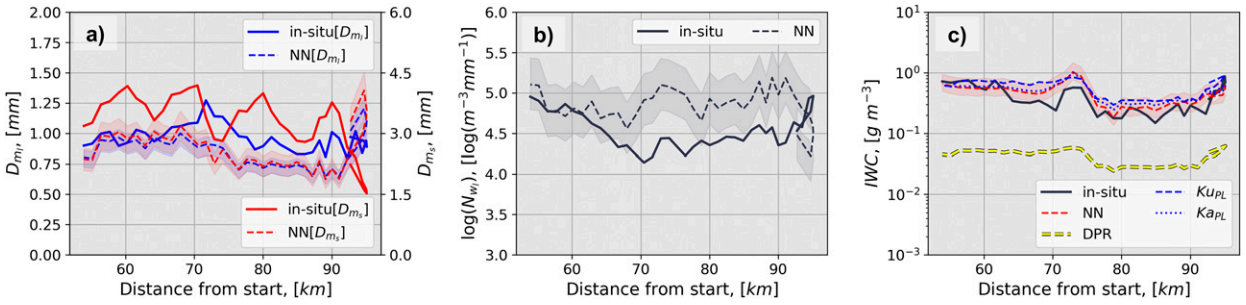

FIG. 14. As in Fig. 8, but for 3 Dec 2015.

relative to a single-frequency power law and an estimate of the current GPM-DPR algorithm.

4. Neural network implementation on GPM-DPR data

One unique aspect of the 3 December 2015 case was that the GPM-DPR overpassed the region during the coordinated flights of the DC-8 and Citation (GPM-DPR orbit track in dotted lines on Fig. 12a). Thus, the GPM-DPR observations and the direct output of the operational algorithm can be compared against the APR data and the output from the NN retrieval. Since the sensitivity of the GPM-DPR is approximately 12 and 18 dBZ for the Ku- and Ka-band normal scan, respectively (Toyoshima et al. 2015), the first noticeable difference between the APR (Fig. 13) and GPM-DPR (Fig. 15) is in echo-top height. In the GPM-DPR data, the echo tops are found at about 5–6 km at Ku band (Fig. 15a) and 4–5 km at Ka band (Fig. 15b) while the APR showed echo tops to about 8 km (Figs. 13a,b). The decrease in along-track resolution and vertical resolution can also be gleaned by comparing Figs. 13a–c and 15a–c. Despite the differences, GPM-DPR measures similar enhancements in DFR_{Ku-Ka} at 4 km altitude and 25–100 km horizontally and from 100 to 125 km horizontally.

Note the current operational GPM-DPR algorithm has an along-track ray-to-ray variability that is consistent throughout the vertical column in the retrieved products (Figs. 15d–f). This likely occurs because the profiles of Z_e are attenuation corrected by considering the surface echo as reference, and this value is used in the microphysical solver to estimate retrieved quantities such as N_{w_l} and D_{m_l} (Iguchi et al. 2018, see their section 3g). Since these observations were collected over complex topography, the estimation of path integrated attenuation using the surface reference technique likely contains large errors resulting in the unphysical retrieval result. Despite this, there does seem to be a local enhancement of D_{m_l} at 4 km between 30 and 50 km (Fig. 15d), which is consistent with the NN retrieval applied to the APR data (Fig. 13d). Looking beyond the ray-to-ray instability, the overall magnitude of N_{w_l} is a factor of 10 lower than what was retrieved by the NN on the APR data, which through Eq. (8) leads to a factor-of-10 lower IWC retrieved by GPM-DPR. This is consistent with the low bias reported by Casella et al. (2017), Heymsfield et al. (2018), Skofronick-Jackson et al. (2019), and Chase et al. (2020) and with the results shown in Figs. 8c, 11c, and 14c.

While it has been shown here that the NN retrieval performs better than the average GPM-DPR retrieval of IWC (section 3) using the APR data, the uncertainties caused by the resolution differences, radar sensitivity differences, and the source of environmental temperature information could impact the retrieval when applied to the GPM-DPR data (e.g., Pfitzenmaier et al. 2019). To investigate how the radar differences impact the retrieval, the NN is applied directly to the GPM-DPR data on the 3 December 2015 (Fig. 16). The first noticeable improvement is the correction of the ray-to-ray variability in retrieved parameters. As a result, the enhancement of D_{m_l} at 4 km becomes more pronounced, showing up continuously in along-track scans (Fig. 16a). The second improvement is the retrieval of N_{w_l}, which has similar magnitude [approximately 5 log(m^{-3} mm^{-1})] as in the APR retrieval (Fig. 13e), leading to similar retrieved IWC values.

To directly compare the results from sections 3 and 4, the median profiles of D_{m_l}, N_{w_l} and IWC for each retrieval are shown in Fig. 17. Note that the means are taken from all scans of the APR, which in areal coverage approximately equal the area of the GPM-DPR. Furthermore, the APR data were constrained to have the same minimum sensitivity of GPM-DPR, which is 12 and 18 dBZ for Ku and Ka band, respectively. Despite the resolution and sensitivity differences, the NN retrieval applied to the GPM-DPR data largely capture the same profile of the NN retrieval applied to the APR. The main differences that occur are that there is an overestimation (+0.03 mm) of D_{m_l} and an underestimation of N_{w_l} [−0.04 log(m^{-3} mm^{-1})] between 2 and 4 km. Since the bias of the retrieval of D_{m_l} and N_{w_l} are of opposite in sign, they largely

TABLE 6. As in Table 4, but for 3 Dec 2015.

Parameter	NN	DDA/GMM Ku, Ka	2ADPR
D_{m_l}, D_{m_s}	0.17, 1.17 mm; (−13%, −25%)	*	*
N_{w_l}	5.56×10^5 m^{-3} mm^{-1}; (+129%)	*	*
IWC	0.16 g m^{-3}; (+13%)	0.22, 0.17 g m^{-3}; (+47%, +35%)	0.42 g m^{-3}; (−89%)

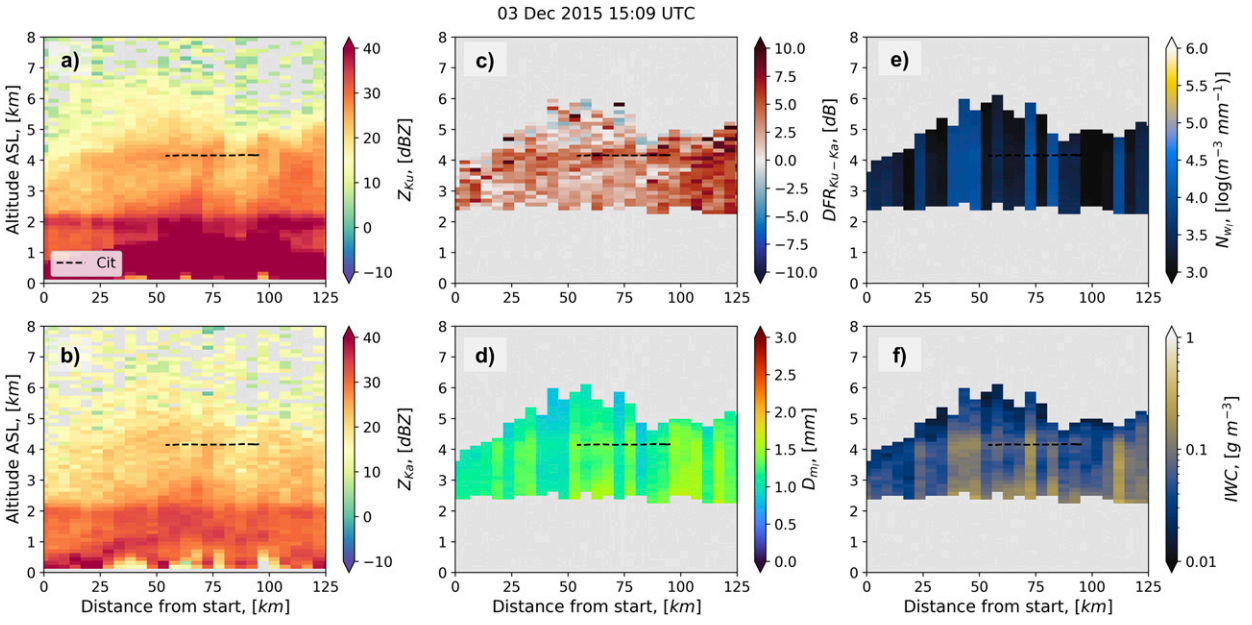

FIG. 15. Similar to Fig. 13, but now using GPM-DPR data along the APR3 swath (scan 9 of the inner swath). (a) Measured Ku-band Z_e. (b) Measured Ka-band Z_e. (c) Measured $\mathrm{DFR_{Ku–Ka}}$. (d) GPM-DPR version-6 retrieved D_{m_l}. (e) GPM-DPR version-6 retrieved N_{w_l}. (f) IWC calculated from the GPM-DPR version-6 retrieval of D_{m_l} and N_{w_l}.

offset in the calculated IWC. The median profiles from the current GPM-DPR algorithm show a constant high bias of D_{m_l} (+0.35 mm), low bias of N_{w_l} [$-1.5\log(\mathrm{m^{-3}\,mm^{-1}})$], and thus a low bias of IWC ($-0.5\,\mathrm{g\,m^{-3}}$). Thus, the NN applied to the GPM-DPR data can provide physically plausible results that are improved relative to the current GPM-DPR retrieval for solid-phase hydrometeor properties.

5. Summary and conclusions

An approach using neural networks (NNs) to retrieve snowfall properties was formulated with a database of more than 20 000 ice particles whose microwave scattering properties were simulated using the discrete dipole approximation and the generalized multiparticle Mie method. The pool of particles was paired with observed particle size distributions (PSDs) measured within ice clouds during NASA Ground Validation field campaigns to produce a synthetic database of snowfall properties and their effective radar reflectivity factor (Z_e) at two frequencies (Ku and Ka band). The synthetic database was used to train an NN to retrieve two parameters of the 3-parameter gamma particle size distribution: the liquid equivalent mass-weighted mean diameter D_{m_l} and the liquid equivalent normalized intercept parameter N_{w_l}, from which the ice water content (IWC) can be calculated following Eq. (8). An evaluation on a subset of the synthetic database not used in training showed the NN retrieval has an RMSE of 0.1 mm, $1.28 \times 10^6\,\mathrm{m^{-3}\,mm^{-1}}$ and $0.24\,\mathrm{g\,m^{-3}}$ with an average range of uncertainty of [−10%, +7%], [−51%, +114%], and [−25%, +43%] for D_{m_l}, N_{w_l}, and IWC, respectively. Furthermore, three simple power-law relations between Z_e and IWC evaluated on the same test dataset show significantly ($p < 0.05$) worse square error on the IWC retrieval relative to the NN.

Three case studies from NASA GV field campaigns provided an independent evaluation of the NN retrieval on coincident observations of Z_e and the PSD. The first case, collected on 31 January 2012, showed that the NN had a median percentage error (MPE) between the retrieval and the in situ

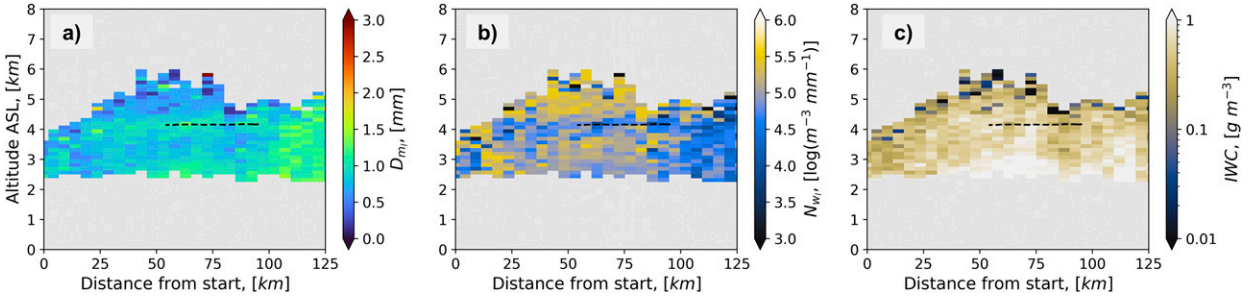

FIG. 16. Neural network retrieval applied to GPM-DPR data for (a) D_{m_l}, (b) N_{w_l}, and (c) IWC.

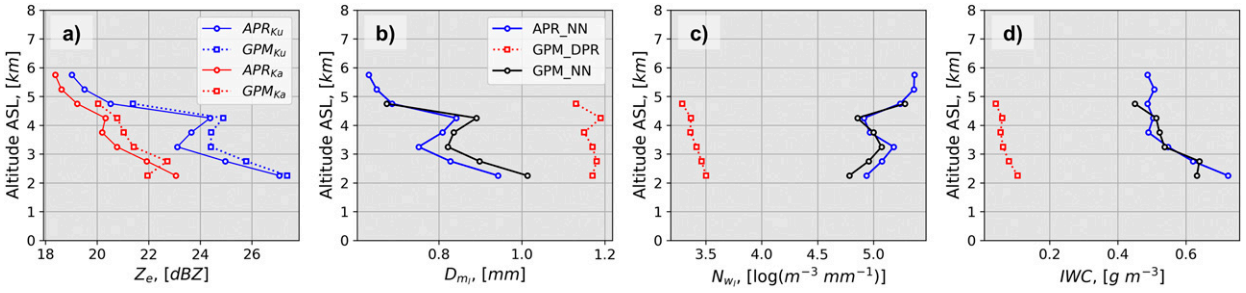

FIG. 17. Median profiles of measured and retrieved microphysical parameters from 1509 UTC 3 Dec 2015: (a) measured median reflectivity from the APR (solid lines) and GPM-DPR (dashed lines) for both Ku (blue) and Ka (red) bands; (b) D_{m_l} retrieved from the neural network applied to the APR data (APR_NN; blue), retrieved from the GPM-DPR version-6 algorithm (GPM_DPR; red), and retrieved from the neural network applied to the GPM-DPR data (GPM_NN; black); (c) As in (b), but for N_{w_l}; and (d) the resulting IWC calculated from D_{m_l} and N_{w_l}.

estimates of +13%, −61%, and −28% for D_{m_l}, N_{w_l}, and IWC, respectively. The second case, a shallow lake effect snowfall event (12 February 2012), showed better performance with MPE of +8% and −48% for D_{m_l} and N_{w_l}, respectively, but worse performance on IWC (MPE of −38%). The third case within a Pacific Northwest cyclone over complex topography (3 December 2015) showed MPE of −13%, +129%, and +13% for D_{m_l}, N_{w_l}, and IWC, respectively. Analysis for all three case studies showed that the NN has significantly lower square error when compared with an estimate of the current GPM-DPR algorithm and a legacy power-law fit between Z_e and IWC. The NN retrieval was applied directly to GPM-DPR observations and indicated that the NN can provide a physically plausible profile, which is able to capture the same microphysical structures of the higher-resolution APR retrieval and correct for undesired retrieval artifacts found in the current GPM-DPR algorithm (e.g., ray-to-ray discontinuity).

This was the first attempt at providing a viable solid-phase retrieval alternative for GPM-DPR. Thus, the retrieval in its current form has caveats that readers and users should be aware of. Currently, there are no rimed particle types included in the training database of particles despite rimed particles being available from the literature (Leinonen and Szyrmer 2015). That being said, the NN retrieval continues to outperform a simple power-law and the GPM-DPR algorithm estimate on case studies where riming is likely present (see the 12 February 2012 and 3 December 2015 cases). In future iterations of the NN retrieval, rimed particle types should be included. Another caveat is that the training data for the NN were informed from three field campaigns all located in North America. Thus, if the goal is to have a global snowfall retrieval, future iterations of the retrieval should look to included additional field campaign measurements of PSDs collected in other precipitation regimes across the globe. A sensitivity analysis using different sources for the temperature input to the retrieval does affect the retrieval by around 10–25%. Thus, for optimal performance of this NN retrieval, users should use the most accurate available temperature input (e.g., Sounding in close proximity spatially and temporally).

Future avenues of research could modify the NN to also predict the shape parameter of the PSD (μ); that way, other PSD characteristics, such as precipitation rate, can be derived. Future work should also look to evaluate the NN retrieval on additional case studies from OLYMPEX, GCPEX and other campaigns (e.g., Petäjä et al. 2016; Lubin et al. 2020) with high-quality coincident multifrequency and microphysical measurements. The additional evaluation would further inform users of the accuracy and potential biases associated with the NN retrieval. Last, the comparison with *CloudSat* and the operational algorithms therein would be beneficial for understanding whether the bias reported in Skofronick-Jackson et al. (2019) and Casella et al. (2017) has been improved with the NN retrieval.

Acknowledgments. Funding for this research was provided to the University of Illinois by NASA Precipitation Measurement Missions Grant 80NSSC19K0713 and NASA Earth System Science Fellowship 80NSSC17K0439. We thank all of the participants of the field campaigns used here for their tireless effort in collecting the data used in this study. Furthermore, we also thank Google Colaboratory for their open-source free computing platform that allowed for the simple implementation of the neural network presented here. We also thank the three anonymous reviewers for the insightful comments that enhanced this paper.

Data availability statement. The amalgamation of DDA/GMM particles used in the formulation of the synthetic data, the synthetic data themselves, and the notebook used to train the neural network are found with the data repository associated with this paper (https://doi.org/10.13012/B2IDB-0791318_V2). The NASA GV field campaign data used in the three case studies can be made available upon request to the corresponding author, or the interested party can obtain all NASA GV data from NASA's Global Hydrology Resource Center (https://ghrc.nsstc.nasa.gov/home/). Version 6 of the GPM-DPR data can be found online (https://doi.org/10.5067/GPM/DPR/GPM/2A/05).

APPENDIX A

Derivation of GPM-DPR estimate

Since the GPM-DPR operational algorithm is not trivial to implement and is not open source, a method to estimate the

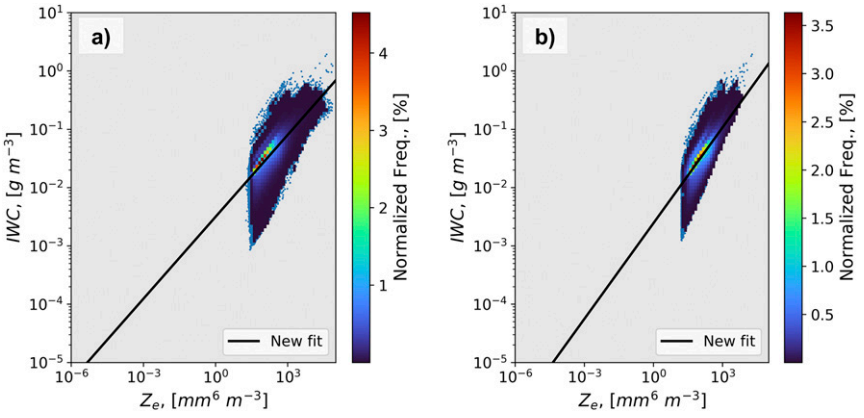

FIG. A1. Randomly selected snowfall echoes from the 2A.DPR files: the (a) Ku-band and (b) Ka-band relationships between Z_e and IWC. Shading is the density of points in each bin, normalized to the total number of points.

GPM-DPR algorithm is described here. A legacy power-law fit of the form in Eq. (9) is formed from direct operational output of the level-2 2A.DPR files (https://doi.org/10.5067/GPM/DPR/GPM/2A/05). Specifically, four orbital files are chosen from 2014, 2015, 2016, 2017, and 2018, resulting in 20 total files. From there, the data are curated by selecting precipitating profiles (flagPrecip = 11) and where the near-surface temperature, determined from the 2A.ENV files, is less than 5°C. The temperature threshold is to prevent strong convective instances in the data where riming would be likely. From there, radar gates are chosen in which the gate temperature is less than 0°C to isolate solid-phase hydrometeors. Figure A1 shows randomly selected snowfall echoes from the 2A.DPR files. After the above conditions have been selected, the parameters in Eq. (10) are fit using the sklearn python package linear regression between the log(IWC) and the log(Z_e). The α and β values can be found in Table 1.

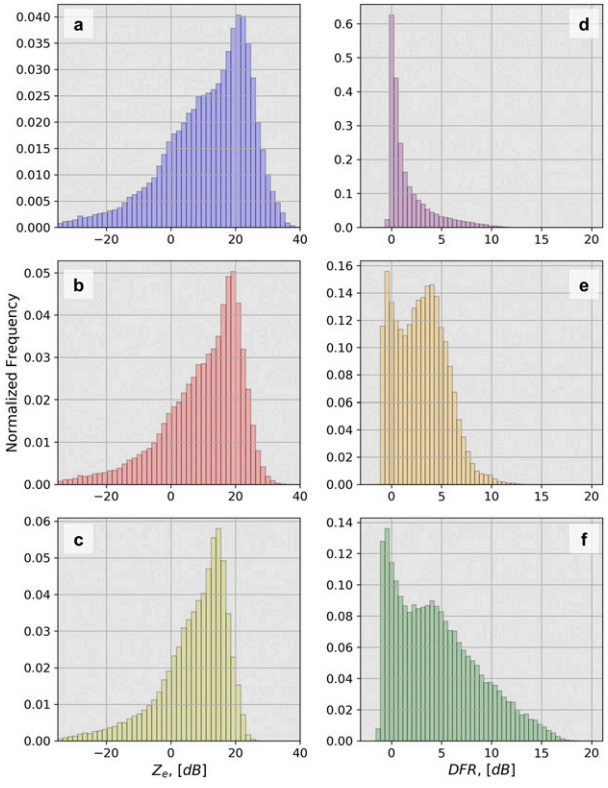

FIG. B1. Histograms of training dataset parameters: (a) Ku band, (b) Ka band, (c) W band, (d) DFR Ku-Ka, (e) DFR Ka-W, and (f) DFR Ku-W.

APPENDIX B

Histograms of training data

To provide perspective of the range of data used to train the neural network, all scattering properties are summarized in normalized histograms in Fig. B1. The left column contains all of the ranges of reflectivity at Ku (Fig. B1a), Ka (Fig. B1b), and W (Fig. B1c) band. The corresponding dual-frequency ratios between Ku and Ka (Fig. B1d), Ka and W (Fig. B1e), and Ku and W (Fig. B1f) are found in the right column.

REFERENCES

Abadi, M., and Coauthors, 2016: TensorFlow: Large-scale machine learning on heterogeneous distributed systems. arXiv 1603.04467, http://arxiv.org/abs/1603.04467.

Abel, S. J., R. J. Cotton, P. A. Barrett, and A. K. Vance, 2014: A comparison of ice water content measurement techniques on the FAAM BAe-146 aircraft. *Atmos. Meas. Tech.*, **7**, 3007–3022, https://doi.org/10.5194/amt-7-3007-2014.

Adhikari, A., and C. Liu, 2019: Geographical distribution of thundersnow events and their properties from GPM Ku-band radar. *J. Geophys. Res. Atmos.*, **124**, 2031–2048, https://doi.org/10.1029/2018JD028839.

——, ——, and M. S. Kulie, 2018: Global distribution of snow precipitation features and their properties from 3 years of GPM observations. *J. Climate*, **31**, 3731–3754, https://doi.org/10.1175/JCLI-D-17-0012.1.

Baumgardner, D., and A. Rodi, 1989: Laboratory and wind tunnel evaluations of the Rosemount icing detector. *J. Atmos. Oceanic*

Technol., **6**, 971–979, https://doi.org/10.1175/1520-0426(1989)006<0971:LAWTEO>2.0.CO;2.

Borque, P., K. J. Harnos, S. W. Nesbitt, and G. M. McFarquhar, 2019: Improved parameterization of ice particle size distributions using uncorrelated mass spectrum parameters: Results from GCPEx. *J. Appl. Meteor. Climatol.*, **58**, 1657–1676, https://doi.org/10.1175/JAMC-D-18-0203.1.

Boucher, R. J., and J. G. Wieler, 1985: Radar determination of snowfall rate and accumulation. *J. Climate Appl. Meteor.*, **24**, 68–73, https://doi.org/10.1175/1520-0450(1985)024<0068:RDOSRA>2.0.CO;2.

Cao, Q., Y. Hong, S. Chen, J. J. Gourley, J. Zhang, and P. E. Kirstetter, 2014: Snowfall detectability of NASA's *CloudSat*: The first cross-investigation of its 2C-snow-profile product and National Multi-Sensor Mosaic QPE (NMQ) snowfall data. *Prog. Electromagn. Res.*, **148**, 55–61, https://doi.org/10.2528/PIER14030405.

Casella, D., G. Panegrossi, P. Sanò, A. C. Marra, S. Dietrich, B. T. Johnson, and M. S. Kulie, 2017: Evaluation of the GPM-DPR snowfall detection capability: Comparison with *CloudSat*-CPR. *Atmos. Res.*, **197**, 64–75, https://doi.org/10.1016/j.atmosres.2017.06.018.

Chase, R. J., and Coauthors, 2018: Evaluation of triple-frequency radar retrieval of snowfall properties using coincident airborne in situ observations during OLYMPEX. *Geophys. Res. Lett.*, **45**, 5752–5760, https://doi.org/10.1029/2018GL077997.

——, S. W. Nesbitt, and G. M. McFarquhar, 2020: Evaluation of the microphysical assumptions within GPM-DPR using ground-based observations of rain and snow. *Atmosphere*, **11**, 619, https://doi.org/10.3390/atmos11060619.

Chen, S., and Coauthors, 2016: Comparison of snowfall estimates from the NASA *CloudSat* Cloud Profiling Radar and NOAA/NSSL Multi-Radar Multi-Sensor System. *J. Hydrol.*, **541**, 862–872, https://doi.org/10.1016/j.jhydrol.2016.07.047.

Delanoë, J., R. J. Hogan, R. M. Forbes, A. Bodas-Salcedo, and T. H. Stein, 2011: Evaluation of ice cloud representation in the ECMWF and UK Met Office models using *CloudSat* and *CALIPSO* data. *Quart. J. Roy. Meteor. Soc.*, **137**, 2064–2078, https://doi.org/10.1002/qj.882.

——, A. J. Heymsfield, A. Protat, A. Bansemer, and R. J. Hogan, 2014: Normalized particle size distribution for remote sensing application. *J. Geophys. Res. Atmos.*, **119**, 4204–4227, https://doi.org/10.1002/2013JD020700.

Delene, D., K. Hibert, M. Poellot, and N. Brackin, 2019: The North Dakota Citation Research Aircraft Measurement Platform. SAE Tech. Paper 2019-01-1990, 13 pp., https://doi.org/10.4271/2019-01-1990.

Ding, S., G. M. McFarquhar, S. W. Nesbitt, R. J. Chase, M. R. Poellot, and H. Wang, 2020: Dependence of mass–dimensional relationships on median mass diameter. *Atmosphere*, **11**, 756, https://doi.org/10.3390/atmos11070756.

Duncan, D., and P. Eriksson, 2018: An update on global atmospheric ice estimates from satellite observations and reanalyses. *Atmos. Chem. Phys.*, **18**, 11 205–11 219, https://doi.org/10.5194/acp-18-11205-2018.

Durden, S. L., S. Tanelli, and O. O. Sy, 2019: Comparison of GPM DPR and airborne radar observations in OLYMPEX. *IEEE Geosci. Remote Sens. Lett.*, **17**, 1707–1711, https://doi.org/10.1109/LGRS.2019.2952287.

Eriksson, P., R. Ekelund, J. Mendrok, M. Brath, O. Lemke, and S. A. Buehler, 2018: A general database of hydrometeor single scattering properties at microwave and sub-millimetre wavelengths. *Earth Syst. Sci. Data*, **10**, 1301–1326, https://doi.org/10.5194/essd-10-1301-2018.

Field, P. R., and A. J. Heymsfield, 2015: Importance of snow to global precipitation. *Geophys. Res. Lett.*, **42**, 9512–9520, https://doi.org/10.1002/2015GL065497.

Finlon, J. A., G. M. McFarquhar, S. W. Nesbitt, R. M. Rauber, H. Morrison, W. Wu, and P. Zhang, 2019: A novel approach for characterizing the variability in mass–dimension relationships: Results from MC3E. *Atmos. Chem. Phys.*, **19**, 3621–3643, https://doi.org/10.5194/acp-19-3621-2019.

Fujiyoshi, Y., T. Endoh, T. Yamada, K. Tsuboki, Y. Tachibana, and G. Wakahama, 1990: Determination of a *Z*–*R* relationship for snowfall using a radar and high sensitivity snow gauges. *J. Appl. Meteor.*, **29**, 147–152, https://doi.org/10.1175/1520-0450(1990)029<0147:DOARFS>2.0.CO;2.

Grecu, M., L. Tiana, G. M. Heymsfield, A. Tokay, W. S. Olson, A. J. Heymsfield, and A. Bansemer, 2018: Nonparametric methodology to estimate precipitating ice from multiple-frequency radar reflectivity observations. *J. Appl. Meteor. Climatol.*, **57**, 2605–2622, https://doi.org/10.1175/JAMC-D-18-0036.1.

Heymsfield, A., A. Bansemer, N. B. Wood, G. Liu, S. Tanelli, O. O. Sy, M. Poellot, and C. Liu, 2018: Toward improving ice water content and snow-rate retrievals from radars. Part II: Results from three wavelength radar–collocated in situ measurements and *CloudSat*–GPM–TRMM radar data. *J. Appl. Meteor. Climatol.*, **57**, 365–389, https://doi.org/10.1175/JAMC-D-17-0164.1.

——, C. Schmitt, C.-C.-J. Chen, A. Bansemer, A. Gettelman, P. R. Field, and C. Liu, 2020: Contributions of the liquid and ice phases to global surface precipitation: Observations and global climate modeling. *J. Atmos. Sci.*, **77**, 2629–2648, https://doi.org/10.1175/JAS-D-19-0352.1.

Hiley, M. J., M. S. Kulie, and R. Bennartz, 2011: Uncertainty analysis for *CloudSat* snowfall retrievals. *J. Appl. Meteor. Climatol.*, **50**, 399–418, https://doi.org/10.1175/2010JAMC2505.1.

Hou, A. Y., and Coauthors, 2014: The Global Precipitation Measurement Mission. *Bull. Amer. Meteor. Soc.*, **95**, 701–722, https://doi.org/10.1175/BAMS-D-13-00164.1.

Houze, R. A., and Coauthors, 2017: The Olympic Mountains Experiment (OLYMPEX). *Bull. Amer. Meteor. Soc.*, **98**, 2167–2188, https://doi.org/10.1175/BAMS-D-16-0182.1.

Iguchi, T., and Coauthors, 2018: GPM/DPR Level-2 Algorithm Theoretical Basis Document. NASA Doc., 127 pp., https://gpm.nasa.gov/sites/default/files/2019-05/ATBD_DPR_201811_with_Appendix3b.pdf.

Jackson, R. C., G. M. McFarquhar, J. Stith, M. Beals, R. A. Shaw, J. Jensen, J. Fugal, and A. Korolev, 2014: An assessment of the impact of antishattering tips and artifact removal techniques on cloud ice size distributions measured by the 2D cloud probe. *J. Atmos. Oceanic Technol.*, **31**, 2567–2590, https://doi.org/10.1175/JTECH-D-13-00239.1.

Jensen, M. P., and Coauthors, 2016: The Midlatitude Continental Convective Clouds Experiment (MC3E). *Bulletin Amer. Meteor. Soc.*, **97**, 1667–1686, https://doi.org/10.1175/BAMS-D-14-00228.1.

Key, J., J. A. Maslanik, and A. J. Schweiger, 1989: Classification of merged AVHRR and SMMR Arctic data with neural networks. *Photogramm. Eng. Remote Sens.*, **55**, 1331–1338.

Kneifel, S., M. S. Kulie, and R. Bennartz, 2011: A triple-frequency approach to retrieve microphysical snowfall parameters. *J. Geophys. Res.*, **116**, D11203, https://doi.org/10.1029/2010JD015430.

Korolev, A., J. W. Strapp, G. A. Isaac, and E. Emery, 2013: Improved airborne hot-wire measurements of ice water

content in clouds. *J. Atmos. Oceanic Technol.*, **30**, 2121–2131, https://doi.org/10.1175/JTECH-D-13-00007.1.

Kozu, T., T. Iguchi, T. Kubota, N. Yoshida, S. Seto, J. Kwiatkowski, and Y. N. Takayabu, 2009: Feasibility of raindrop size distribution parameter estimation with TRMM precipitation radar. *J. Meteor. Soc. Japan*, **87A**, 53–66, https://doi.org/10.2151/jmsj.87A.53.

Kulie, M. S., and R. Bennartz, 2009: Utilizing spaceborne radars to retrieve dry snowfall. *J. Appl. Meteor. Climatol.*, **48**, 2564–2580, https://doi.org/10.1175/2009JAMC2193.1.

——, and L. Milani, 2018: Seasonal variability of shallow cumuliform snowfall: A *CloudSat* perspective. *Quart. J. Roy. Meteor. Soc.*, **144**, 329–343, https://doi.org/10.1002/qj.3222.

——, ——, N. B. Wood, S. A. Tushaus, R. Bennartz, and T. S. L'Ecuyer, 2016: A shallow cumuliform snowfall census using spaceborne radar. *J. Hydrometeor.*, **17**, 1261–1279, https://doi.org/10.1175/JHM-D-15-0123.1.

——, ——, ——, and T. S. L'Ecuyer, 2020: Global snowfall detection and measurement. *Satellite Precipitation Measurement*, Springer, 699–716, https://doi.org/10.1007/978-3-030-35798-6_12.

Kuo, K. S., and Coauthors, 2016: Full access the microwave radiative properties of falling snow derived from nonspherical ice particle models. Part I: An extensive database of simulated pristine crystals and aggregate particles, and their scattering properties. *J. Appl. Meteor. Climatol.*, **55**, 691–708, https://doi.org/10.1175/JAMC-D-15-0130.1.

Langille, R. C., and R. S. Thain, 1951: Some quantitative measurements of three-centimeter radar echoes from falling snow. *Can. J. Phys.*, **29**, 482–490, https://doi.org/10.1139/p51-052.

Leinonen, J., 2014: High-level interface to T-matrix scattering calculations: Architecture, capabilities and limitations. *Opt. Express*, **22**, 1655, https://doi.org/10.1364/OE.22.001655.

——, and D. Moisseev, 2015: What do triple-frequency radar signatures reveal about aggregate snowflakes? *J. Geophys. Res. Atmos.*, **120**, 229–239, https://doi.org/10.1002/2014JD022072.

——, and W. Szyrmer, 2015: Radar signatures of snowflake riming: A modeling study. *Earth Space Sci.*, **2**, 346–358, https://doi.org/10.1002/2015EA000102.

——, and Coauthors, 2018: Retrieval of snowflake microphysical properties from multifrequency radar observations. *Atmos. Meas. Tech.*, **11**, 5471–5488, https://doi.org/10.5194/amt-11-5471-2018.

Liu, C. L., and A. J. Illingworth, 2000: Toward more accurate retrievals of ice water content from radar measurements of clouds. *J. Appl. Meteor.*, **39**, 1130–1146, https://doi.org/10.1175/1520-0450(2000)039<1130:TMAROI>2.0.CO;2.

Liu, G., 2008: Deriving snow cloud characteristics from *CloudSat* observations. *J. Geophys. Res.*, **113**, D00A09, https://doi.org/10.1029/2007JD009766.

Lu, Y., Z. Jiang, K. Aydin, J. Verlinde, E. Clothiaux, and G. Botta, 2016: A polarimetric scattering database for non-spherical ice particles at microwave wavelengths. *Atmos. Meas. Tech.*, **9**, 5119–5134, https://doi.org/10.5194/amt-9-5119-2016.

Lubin, D., and Coauthors, 2020: The Atmospheric Radiation Measurement (ARM) West Antarctic Radiation Experiment. *Bull. Amer. Meteor. Soc.*, **101**, E1069–E1091, https://doi.org/10.1175/BAMS-D-18-0278.1.

Mas, J. F., and J. J. Flores, 2008: The application of artificial neural networks to the analysis of remotely sensed data. *Int. J. Remote Sens.*, **29**, 617–663, https://doi.org/10.1080/01431160701352154.

Matrosov, S. Y., 1992: Radar reflectivity in snowfall. *IEEE Trans. Geosci. Remote Sens.*, **30**, 454–461, https://doi.org/10.1109/36.142923.

McFarquhar, G. M., M. S. Timlin, R. M. Rauber, B. F. Jewett, J. A. Grim, and D. P. Jorgensen, 2007: Vertical variability of cloud hydrometeors in the stratiform region of mesoscale convective systems and bow echoes. *Mon. Wea. Rev.*, **135**, 3405–3428, https://doi.org/10.1175/MWR3444.1.

——, and Coauthors, 2017: Processing of ice cloud in situ data collected by bulk water, scattering, and imaging probes: Fundamentals, uncertainties, and efforts toward consistency. *Ice Formation and Evolution in Clouds and Precipitation: Measurement and Modeling Challenges*, *Meteor. Monogr.*, No. 58, Amer. Meteor. Soc., https://doi.org/10.1175/AMSMONOGRAPHS-D-16-0007.1.

Milani, L., and Coauthors, 2018: *CloudSat* snowfall estimates over Antarctica and the Southern Ocean: An assessment of independent retrieval methodologies and multi-year snowfall analysis. *Atmos. Res.*, **213**, 121–135, https://doi.org/10.1016/j.atmosres.2018.05.015.

Mishchenko, M. I., and L. D. Travis, 1998: Capabilities and limitations of a current FORTRAN implementation of the T-matrix method for randomly oriented, rotationally symmetric scatterers. *J. Quant. Spectrosc. Radiat. Transfer*, **60**, 309–324, https://doi.org/10.1016/S0022-4073(98)00008-9.

Norin, L., A. Devasthale, T. S. L'Ecuyer, N. B. Wood, and M. Smalley, 2015: Intercomparison of snowfall estimates derived from the *CloudSat* Cloud Profiling Radar and the ground-based weather radar network over Sweden. *Atmos. Meas. Tech.*, **8**, 5009–5021, https://doi.org/10.5194/amt-8-5009-2015.

Oliphant, T., 2007: Python for scientific computing. *Comput. Sci. Eng.*, **9**, 10–20, https://doi.org/10.1109/MCSE.2007.58.

Ori, D., V. Schemann, M. Karrer, J. D. Neto, L. von Terzi, A. Seifert, and S. Kneifel, 2020: Evaluation of ice particle growth in ICON using statistics of multi-frequency Doppler cloud radar observations. *Quart. J. Roy. Meteor. Soc.*, **146**, 3830–3849, https://doi.org/10.1002/qj.3875.

Palerme, C., J. Kay, C. Genthon, T. L'Ecuyer, N. Wood, and C. Claud, 2014: How much snow falls on the Antarctic ice sheet? *Cryosphere*, **8**, 1577–1587, https://doi.org/10.5194/tc-8-1577-2014.

——, C. Genthon, C. Claud, J. E. Kay, N. B. Wood, and T. L'Ecuyer, 2017: Evaluation of current and projected Antarctic precipitation in CMIP5 models. *Climate Dyn.*, **48**, 225–239, https://doi.org/10.1007/s00382-016-3071-1.

Petäjä, T., and Coauthors, 2016: A field campaign to elucidate the impact of biogenic aerosols on clouds and climate. *Bull. Amer. Meteor. Soc.*, **97**, 1909–1928, https://doi.org/10.1175/BAMS-D-14-00199.1.

Petersen, W. A., P.-E. Kirstetter, J. Wang, D. B. Wolff, and A. Tokay, 2020: The GPM Ground Validation program. *Satellite Precipitation Measurement*, Vol. 2, Springer, 471–502, https://doi.org/10.1007/978-3-030-35798-6_2.

Pfitzenmaier, L., A. Battaglia, and P. Kollias, 2019: The impact of the radar-sampling volume on multiwavelength spaceborne radar measurements using airborne radar observations. *Remote Sens.*, **11**, 2263, https://doi.org/10.3390/rs11192263.

Plummer, D. M., G. M. McFarquhar, R. M. Rauber, B. F. Jewett, and D. C. Leon, 2015: Microphysical properties of convectively generated fall streaks within the stratiform comma head region of continental winter cyclones. *J. Atmos. Sci.*, **72**, 2465–2483, https://doi.org/10.1175/JAS-D-14-0354.1.

Rodgers, C. D., 2000: *Inverse Methods for Atmospheric Sounding: Theory and Practice*. Vol. 2, Atmospheric, Oceanic and Planetary Physics, World Scientific, 256 pp.

Sadowy, G., A. Berkun, W. Chun, E. Im, and S. Durden, 2003: Development of an advanced airborne precipitation radar. *Microwave J.*, **46**, 84–98.

Sassen, K., 1987: Ice cloud content from radar reflectivity. *J. Climate Appl. Meteor.*, **26**, 1050–1053, https://doi.org/10.1175/1520-0450(1987)026<1050:ICCFRR>2.0.CO;2.

Sekelsky, S. M., W. L. Ecklund, J. M. Firda, K. S. Gage, and R. E. McIntosh, 1999: Particle size estimation in ice-phase clouds using multifrequency radar reflectivity measurements at 95, 33, and 2.8 GHz. *J. Appl. Meteor.*, **38**, 5–28, https://doi.org/10.1175/1520-0450(1999)038<0005:PSEIIP>2.0.CO;2.

Skofronick-Jackson, G., and Coauthors, 2015: Global Precipitation Measurement Cold Season Precipitation Experiment (GCPEX): For measurement's sake, let it snow. *Bull. Amer. Meteor. Soc.*, **96**, 1719–1741, https://doi.org/10.1175/BAMS-D-13-00262.1.

——, M. Kulie, L. Milani, S. J. Munchak, N. B. Wood, and V. Levizzani, 2019: Satellite estimation of falling snow: A Global Precipitation Measurement (GPM) *Core Observatory* perspective. *J. Appl. Meteor. Climatol.*, **58**, 1429–1448, https://doi.org/10.1175/JAMC-D-18-0124.1.

Souverijns, N., and Coauthors, 2018: Evaluation of the *CloudSat* surface snowfall product over Antarctica using ground-based precipitation radars. *Cryosphere*, **12**, 3775–3789, https://doi.org/10.5194/tc-12-3775-2018.

Stein, T. H., D. J. Parker, R. J. Hogan, C. E. Birch, C. E. Holloway, G. M. Lister, J. H. Marsham, and S. J. Woolnough, 2015: The representation of the West African monsoon vertical cloud structure in the Met Office Unified Model: An evaluation with *CloudSat*. *Quart. J. Roy. Meteor. Soc.*, **141**, 3312–3324, https://doi.org/10.1002/qj.2614.

Stephens, G. L., and Coauthors, 2002: The *CloudSat* mission and the A-Train: A new dimension of space-based observations of clouds and precipitation. *Bulletin Amer. Meteor. Soc.*, **83**, 1771–1790, https://doi.org/10.1175/BAMS-83-12-1771.

Tanelli, S., S. L. Durden, and E. Im, 2006: Simultaneous measurements of ku- and ka-band sea surface cross sections by an airborne radar. *IEEE Geosci. Remote Sens. Lett.*, **3**, 359–363, https://doi.org/10.1109/LGRS.2006.872929.

Testud, J., S. Oury, R. A. Black, P. Amayenc, and X. Dou, 2001: The concept of ''normalized'' distribution to describe raindrop spectra: A tool for cloud physics and cloud remote sensing. *J. Appl. Meteor.*, **40**, 1118–1140, https://doi.org/10.1175/1520-0450(2001)040<1118:TCONDT>2.0.CO;2.

Toyoshima, K., H. Masunaga, and F. A. Furuzawa, 2015: Early evaluation of Ku- and Ka-band sensitivities for the Global Precipitation Measurement (GPM) Dual-Frequency Precipitation Radar (DPR). *SOLA*, **11**, 14–17, https://doi.org/10.2151/sola.2015-004.

Tridon, F., and Coauthors, 2019: The microphysics of stratiform precipitation during OLYMPEX: Compatibility between triple-frequency radar and airborne in situ observations. *J. Geophys. Res. Atmos.*, **124**, 8764–8792, https://doi.org/10.1029/2018JD029858.

von Lerber, A., D. Moisseev, L. F. Bliven, W. Petersen, A. M. Harri, and V. Chandrasekar, 2017: Microphysical properties of snow and their link to Z_e–S relations during BAECC 2014. *J. Appl. Meteor. Climatol.*, **56**, 1561–1582, https://doi.org/10.1175/JAMC-D-16-0379.1.

Wood, N. B., and T. S. L'Ecuyer, 2021: What millimeter-wavelength radar reflectivity reveals about snowfall: An information-centric analysis. *Atmos. Meas. Tech.*, **14**, 869–888, https://doi.org/10.5194/amt-14-869-2021.

——, ——, D. G. Vane, G. L. Stephens, and P. Partain, 2013: Level 2C snow profile process description and interface control document, version 0. NASA *CloudSat* Project Doc., 21 pp., http://www.cloudsat.cira.colostate.edu/sites/default/files/products/files/2C-SNOW-PROFILE_PDICD.P_R04.20130210.pdf.

Xiao, R. V. Chandrasekar, and H. Liu, 1998: Development of a neural network based algorithm for radar snowfall estimation. *IEEE Trans. Geosci. Remote Sens.*, **36**, 716–724, https://doi.org/10.1109/36.673664.

Xu, Y. L., 1995: Electromagnetic scattering by an aggregate of spheres. *Appl. Opt.*, **34**, 4573–4588, https://doi.org/10.1364/AO.34.004573.

Yurkin, M. A., and A. G. Hoekstra, 2011: The discrete-dipole-approximation code ADDA: Capabilities and known limitations. *J. Quant. Spectrosc. Radiat. Transfer*, **112**, 2234–2247, https://doi.org/10.1016/j.jqsrt.2011.01.031.